

SEARCH FOR RESONANT DOUBLE HIGGS PRODUCTION WITH $b\bar{b}Z\bar{Z}$
DECAYS IN THE $b\bar{b}\ell\ell\nu\bar{\nu}$ FINAL STATE IN pp COLLISIONS AT $\sqrt{s} = 13$ TeV

by

Rami Kamalieddin

A DISSERTATION

Presented to the Faculty of
The Graduate College at the University of Nebraska
In Partial Fulfilment of Requirements
For the Degree of Doctor of Philosophy

Major: Physics and Astronomy

Under the Supervision of Professor Ilya Kravchenko

Lincoln, Nebraska

May, 2019

SEARCH FOR RESONANT DOUBLE HIGGS PRODUCTION WITH $b\bar{b}Z\bar{Z}$
DECAYS IN THE $b\bar{b}\ell\ell\nu\bar{\nu}$ FINAL STATE IN pp COLLISIONS AT $\sqrt{s} = 13$ TeV

Rami Kamalieddin, Ph.D.

University of Nebraska, 2019

Adviser: Ilya Kravchenko

Since the discovery of the Higgs boson in 2012 by the ATLAS and CMS experiments, most of the quantum mechanical properties that describe the long-awaited Higgs boson have been measured. Due to the outstanding work of the LHC, over a hundred of fb^{-1} of proton collisions data have been delivered to both experiments. Finally, it became sensible for analyses teams to start working with a very low cross section processes involving the Higgs boson, e.g., a recent success in observing $t\bar{t}H$ and $VHbb$ processes. One of the main remaining untouched topics is a double Higgs boson production. However, an additional hundred of fb^{-1} per year from the HL-LHC will not necessarily help us much with the SM double Higgs physics, as the process may remain unseen even in the most optimistic scenarios. The solution is to work in parallel on new reconstruction and signal extraction methods as well as new analysis techniques to improve the sensitivity of measurements. This thesis is about both approaches: we have used the largest available dataset at the time the analysis has been performed and developed/used the most novel analysis methods. One such method is the new electron identification algorithm that we have developed in the CMS electron identification group, to which I have had a privilege to contribute during several years of my stay at CERN.

The majority of this thesis is devoted to techniques for the first search at the LHC for double Higgs boson production mediated by a heavy narrow-width resonance in

the $b\bar{b}ZZ$ channel: $X \rightarrow HH \rightarrow b\bar{b}ZZ^* \rightarrow b\bar{b}\ell\ell\nu\bar{\nu}$. The measurement searches for the resonant production of a Higgs boson pair in the range of masses of the resonant parent particle from 250 to 1000 GeV using 35.9 fb^{-1} of data taken in 2016 at 13 TeV. Two spin scenarios of the resonance are considered: spin 0 and spin 2. In the absence of the evidence of the resonant double Higgs boson production from the previous searches, we proceed with setting the upper confidence limits.

“You keep writing, we will keep reading”

Ken Bloom, 2018.

ACKNOWLEDGMENTS

This will be a long list!

Table of Contents

List of Figures	viii
List of Tables	xii
1 <i>bbZZ</i> Physics Analysis	1
1.1 Physics analysis overview	1
1.2 Data analysis strategy	3
1.3 Data and Triggers	4
1.3.1 Data	4
1.3.2 Triggers	4
1.4 Simulated Samples	9
1.4.1 Signal processes simulation	9
1.4.2 Background processes simulation	10
1.5 Physics Objects Selection	12
1.5.1 Electrons	13
1.5.2 Muons	13
1.5.3 Jets	14
1.5.4 b jets	14
1.5.5 Missing transverse momentum	15

1.6	Event Selection	15
1.6.1	Kinematic selection of physics objects	16
1.6.2	Signal candidate construction and selection	18
1.6.3	Signal and control kinematic regions	20
1.6.4	Signal region candidate selection with a multivariate technique	22
1.7	Multivariate selection in the signal region	22
1.7.1	Kinematic variables of a candidate	23
1.7.2	Multivariate discriminant: a BDT classifier	33
1.7.3	BDT selection requirement in the signal region	53
1.8	Systematic Uncertainties	54
1.8.1	Normalization uncertainties	55
1.8.2	Shape uncertainties	57
1.9	Statistical Analysis	59
1.10	Limits Extraction	60
1.10.1	Results from the fit	61
1.11	$bbZZ$ measurements and combination of all HH channels	63
1.11.1	Data and MC comparison	66
1.11.2	Scale Factors	68
2	Conclusions	75
	Bibliography	77
	References	77

List of Figures

1.1	HLT trigger SFs for electrons.	7
1.2	Final HLT SFs for muons as a function of p_T and η , measured for eras B to G.	8
1.3	Final HLT SFs for muons as a function of p_T and η , measured for the era H.	8
1.4	SFs for muons of the dZ requirement	9
1.5	Optimisation of the MET selection for two $bbZZ$ analyses	17
1.6	Signal region, control region $t\bar{t}$, and control region Drell-Yan in the phase space of $Z \rightarrow \ell\ell$ and $H \rightarrow b\bar{b}$ masses.	21
1.7	Comparison of data and MC samples. 300 GeV, CRDY region, mm chan- nel. Prefit plot on the left, Full Postfit plot on the right.	27
1.8	Comparison of data and MC samples. 300 GeV, CRDY region, mm chan- nel. Prefit plot on the left, Full Postfit plot on the right.	28
1.9	Comparison of data and MC samples. 300 GeV, SR region, mm channel. Prefit plot on the left, Full Postfit plot on the right.	29
1.10	Comparison of data and MC samples. 300 GeV, SR region, mm channel. Prefit plot on the left, Full Postfit plot on the right.	30
1.11	Comparison of data and MC samples. 300 GeV, CRTT region, mm chan- nel. Prefit plot on the left, Full Postfit plot on the right.	31

1.12	Comparison of data and MC samples. 300 GeV, CRTT region, mm channel. Prefit plot on the left, Full Postfit plot on the right.	32
1.13	BDT trees 1 and 2 (indexing starts from 0). These trees relied on: the mass and the p_T of the $Z(\ell\ell)$ candidate, ΔR separation between two b jets, the mass of the $H \rightarrow b\bar{b}$ candidate, and the p_T of the ZZ^* system. The TMVA notation is explained in 1.7.2.	37
1.14	BDT trees 400 and 401 (indexing starts from 0). These trees relied on: the p_T of the $Z(\ell\ell)$ candidate, ΔR separation between two b jets, ΔR separation between two charged leptons, the p_T of the $H \rightarrow b\bar{b}$ candidate, and the mass and the p_T of the ZZ^* system. The TMVA notation is explained in 1.7.2.	38
1.15	BDT trees 799 and 800 (indexing starts from 0). These trees relied on: the p_T of the $Z(\ell\ell)$ candidate, ΔR separation between two b jets, ΔR separation between two charged leptons, the mass of the $H \rightarrow b\bar{b}$ candidate, and the mass of the ZZ^* system. The TMVA notation is explained in 1.7.2.	39
1.16	Input variable correlations of the di-electron channel, low mass training. Top: signal sample mix. Bottom: background sample mix. The TMVA notation is explained in 1.7.2.	43
1.17	Input variable correlations of the di-electron channel, high mass training. Top: signal sample mix. Bottom: background sample mix. The TMVA notation is explained in 1.7.2.	44
1.18	Variables used in the low mass training for di-electron channel. Index '1' refers to $H \rightarrow b\bar{b}$ decay and index '0' refers to $H \rightarrow ZZ$ decay. The TMVA notation is explained in 1.7.2.	45

1.19	Variables used in the high mass training for di-electron channel. Index '1' refers to $H \rightarrow b\bar{b}$ decay and index '0' refers to $H \rightarrow ZZ$ decay. The TMVA notation is explained in 1.7.2.	46
1.20	BDT discriminants for di-electron channel. Top: low mass training. Bottom: high mass training.	48
1.21	ROC curves for di-electron channel. Top: low mass training. Bottom: high mass training.	50
1.22	BDT distributions for the radion case, electron(muon) channel is shown at the top(bottom). Signal region is presented, 300 GeV mass hypothesis. For electrons the selection is at 0.4, for muons at 0.7, as is described in Section 1.7.3.	52
1.24	Combination of HH channels using 2016 data. Expected (dashed) and observed (solid line) 95% CL exclusion limits are shown. The results describe the production cross section of a narrow width spin 0 (top) and spin 2 (bottom) resonance decaying into a pair of SM Higgs bosons. . .	66
1.23	Expected (dashed line) and observed (solid line) limits on the cross section of a resonant HH production as a function of the mass of the narrow resonance for both leptonic channels combined. Graviton case is shown at the top and radion case at the bottom. The red line shows a theoretical prediction for the production of a WED particle with certain model assumptions [2].	69
1.25	Muon ID scale factors in p_T and η bins. Left: runs B to F. Right: runs G and H.	70
1.26	Muon ISO scale factors in p_T and η bins. Left: runs B to F. Right: runs G and H.	71
1.27	Electron ID+ISO scale factors in p_T and η bins.	72

1.28	Cut flow for mm (top) and ee (bottom) channels.	73
1.29	Transverse mass of the reconstructed HH candidates for data, the simulated signal graviton sample for the 300 GeV mass hypothesis, and simulated backgrounds scaled according to the fit results. The top row shows the figures for the muon channel while the bottom row is for the electron channel. For each row, the left plot is for the Drell-Yan control region, the middle is for the $t\bar{t}$ control region, and the right is for the signal region. Signal normalization choice is discussed in the text. The crosshatched area represents the sum of statistical and systematic uncertainties.	73
1.30	Transverse mass of the reconstructed HH candidates for data, the simulated signal radion sample for the 300 GeV mass hypothesis, and simulated backgrounds scaled according to the fit results. The top row shows the figures for the muon channel while the bottom row is for the electron channel. For each row, the left plot is for the Drell-Yan control region, the middle is for the $t\bar{t}$ control region, and the right is for the signal region. Signal normalization choice is discussed in the text. The crosshatched area represents the sum of statistical and systematic uncertainties.	74

List of Tables

1.1	List of used data sets collected by the CMS in 2016. Each era contains a unique letter identifier and also specifies the date when the data processing was done. If the re-processing was run, the name contains the word ending “v2”. Corresponding integrated luminosities are shown in the second column.	4
1.2	Background Monte Carlo samples	11
1.3	The MET requirements as a function of the mass of the HH candidate. Selection values (the second column) are provided for different mass hypotheses (the first column) of the narrow resonance decaying to the HH system.	18
1.4	Number of events surviving the candidate selection and kinematic requirements. Numbers are given for $bbZZ$ and $bbWW$ contributions in the SR. Efficiency values are also provided (the third column) and are normalised to the initial event counts before any selection is applied. Di-muon channel is presented. Numbers for di-electron channel have the same trend but lower values since in the CMS, efficiencies for electrons are lower than for muons.	22

1.5	Di-electron channel. Relative importance of the input variables in the low mass BDT training.	40
1.6	Di-electron channel. Relative importance of the input variables in the high mass BDT training.	41
1.8	Di-muon channel. Relative importance of the input variables in the high mass BDT training.	41
1.7	Di-muon channel. Relative importance of the input variables in the low mass BDT training.	41
1.9	The BDT selection values used in this measurement.	53
1.10	Efficiency of the BDT selection requirement. ee channel (top) and $\mu\mu$ channel (bottom).	54
1.11	The expected and observed HH production cross section upper limits at 95% CL for different narrow resonance graviton (top) and radion (bottom) mass hypotheses for both dielectron and dimuon channels combined. . .	62

CHAPTER 1

bbZZ Physics Analysis

In this chapter, we report on a search for the resonant production of the double Higgs boson system. Higgs boson pairs subsequently decay through the $bbZZ$ channel. The final state consists of two b jets, two charged leptons, and two neutrinos ($2b2l2\nu$ final state). Analysed data set was collected in 2016 by the CMS experiment in proton-proton collisions at 13 TeV COM energy, and corresponds to 35.9 fb^{-1} of the integrated luminosity.

1.1 Physics analysis overview

We search for di-Higgs production through the gluon fusion mechanism mediated by two types of possible heavy resonances (separately): a spin-2 Randall-Sundrum (RS1) Kaluza-Klein (KK) graviton and a spin-0 RS1 radion [44, 52]. The width of the graviton and radion is assumed to be negligible with respect to the experimental resolution. We look for decays of WED particles (X) to the $bbZZ$ and $bbWW$ channels with the two b jets, two charged leptons, and two neutrinos final state $X \rightarrow HH \rightarrow bbZZ/bbWW \rightarrow 2b2l2\nu$. In the above, one of the Higgs bosons decays to a pair of b quarks and the other Higgs boson decays to ZZ or WW system. We consider only leptonic decays of ZZ and WW. Intermediate taus are allowed to decay to daughter

muons and electrons. We explore the invariant masses of WED particles ranging from 250 to 1000 GeV. The result of the measurement is the production cross section of the resonance times the branching fraction of its decay into the aforementioned $2b2l2\nu$ final state.

In this data analysis (later referred to as the analysis), we will describe first the data sets (often referred to as a dataset) and triggers. The measurement uses the DoubleEG and DoubleMuon PDs defined in the previous chapter. These di-electron and di-muon channels are analysed separately and the information is combined in the final result. To select the events with two prompt charged leptons, a set of triggers is applied. To increase the statistics of the measurement and maximise the number of leptons passing the selection, certain complex trigger strategies are employed.

We continue then with the discussion on the MC simulation of the signal and background processes (later referred to as signal and background). The signal MC samples had to be produced for both graviton and radion particles for 16 mass points from 250 to 1000 GeV to cover the whole search range.

The description of the physics object reconstruction and event selection is given. Physics objects are constructed using the information from the CMS subsystems and the output of the PF algorithm. Then, based on the final state signature, the events are selected containing corresponding physics objects. The construction of the Higgs and Z boson candidates is discussed at length. The characteristics of signal and background processes are specified and data-MC SFs are discussed.

MVA technique is used to improve signal-background discrimination. We rely on the BDT classifier to reduce the contribution of the background processes in the signal-enriched regions. In all physics measurements, there are sources of the systematic and statistical uncertainties that affect the final results. We discuss all major uncertainties at length and specify the size of the effect of individual types of uncer-

tainties on the final result.

We present the statistical analysis used to extract the results of the measurements and discuss the CMS statistical package that has been used to extract the final results. Then, we present the results of the measurement and compare them with the theory predictions. Finally, we discuss the “grand HH combination” using measurements of all available HH channels.

The material in this chapter follows the description of two articles to which the author contributed directly [159, 181].

1.2 Data analysis strategy

We form the Lorentz energy-momentum vector associated with the double Higgs system. This vector is constructed as the sum of the Lorentz vectors of the two leptons, two b-jets, and the four-vector representing neutrinos (\cancel{p}_T). As the z component of the neutrinos' momentum is unknown, we proceed forming a pseudo transverse mass: $\tilde{M}_T(HH) = \sqrt{E^2 - p_z^2}$ (further referred to as transverse mass for brevity), where E and p_z are the energy and the z axis component of the Lorentz energy-momentum vector of the di-Higgs candidate.

The $\tilde{M}_T(HH)$ distributions are derived for 16 mass and for both spin hypotheses. The $\tilde{M}_T(HH)$ is constructed using the signal and background simulations. The distributions are produced separately for the signal-enriched (SR) and control regions (CR), which are defined later in this chapter.

To extract the final results, we perform a simultaneous fit of the sum of the signal and background $\tilde{M}_T(HH)$ distributions in the SR and CRs to the data. The fits are produced for both di-electron and di-muon channels and the results are combined. We obtain 95% CL upper limits on the HH production cross times the BFs of the

subsequent decay to the final state of this measurement. The employed statistical method is based on the CL_S asymptotic procedure [107].

1.3 Data and Triggers

1.3.1 Data

The search is performed using DoubleMuon and DoubleEG PDs corresponding to an integrated luminosity of 35.9 fb^{-1} recorded by the CMS experiment during Run 2 in 2016. The data were produced in proton-proton collisions at the LHC at 13 TeV COM energy. The data were collected in several data taking periods and approximate values of the integrated luminosity of these periods are given in the Table 1.1.

Table 1.1: List of used data sets collected by the CMS in 2016. Each era contains a unique letter identifier and also specifies the date when the data processing was done. If the re-processing was run, the name contains the word ending “v2”. Corresponding integrated luminosities are shown in the second column.

Dataset	$\int \mathcal{L} \text{ (fb}^{-1}\text{)}$
Run2016B-03Feb2017-v2	~ 5.9
Run2016C-03Feb2017-v1	~ 2.7
Run2016D-03Feb2017-v1	~ 4.3
Run2016E-03Feb2017-v1	~ 4.1
Run2016F-03Feb2017-v1	~ 3.2
Run2016G-03Feb2017-v1	~ 3.8
Run2016H-03Feb2017-v1	~ 11.8
Total Luminosity	35.9

1.3.2 Triggers

The data events that are used in this measurement are selected with a set of HLT triggers, each requiring the presence of two muons or two electrons in the event. In the di-electron final state, the trigger requires the leading electron to have the p_T above

23 GeV, and the sub-leading electron to have the p_T above 12 GeV. The latter leg corresponds to a relatively low efficiency electron. Since the measurement is focused on “golden” electrons coming from on-shell Z boson decays, the offline selection is slightly tighter than the HLT selection and requires the sub-leading electron to have the p_T above 15 GeV.

The final state that contains two prompt muons is selected with the HLT path that is a combination of several HLT paths chained using the logical “OR” operation, in other words, the muons are required to pass the selection of at least one of the HLT paths. At the HLT level, the leading and the sub-leading muons have to pass 17 and 8 GeV p_T requirements respectively. The difference among HLT paths has been explained at length in the Section ???. The offline analysis increases the p_T threshold values to 20 and 15 GeV correspondingly. For the offline selection, electrons are selected in the range $\eta < 2.5$ and muons in the range $\eta < 2.4$. For both channels, the η region in the gap (1.4442 to 1.566) between the barrel and endcap is excluded.

The same trigger selections are applied to MC simulated events. The efficiencies are then derived for MC and data, and SFs are determined using the TnP procedure discussed in Section ???. Trigger SFs have been computed for each trigger leg separately, since the selection of each leg varies (Fig. 1.1). Following the recommendations from the CMS Muon POG, scale factors have been calculated separately for two data collecting periods: runs B to G (Fig. 1.2, and run H separately (Fig. 1.3), since the LHC conditions varied significantly for the run H. All eras have slightly different integrated luminosities, see Table ??, so the final SFs are luminosity averaged. Additionally, as was discussed in the chapter on CMS Physics Objects Reconstruction, some triggers did not contain DZ requirement, while others did. Therefore, scale factors of the DZ selection are also measured, see Fig. 1.4). Prior to measuring the trigger scale factors, the electrons and muons were required to satisfy ID and ISO

selections, more in the subsections ??.

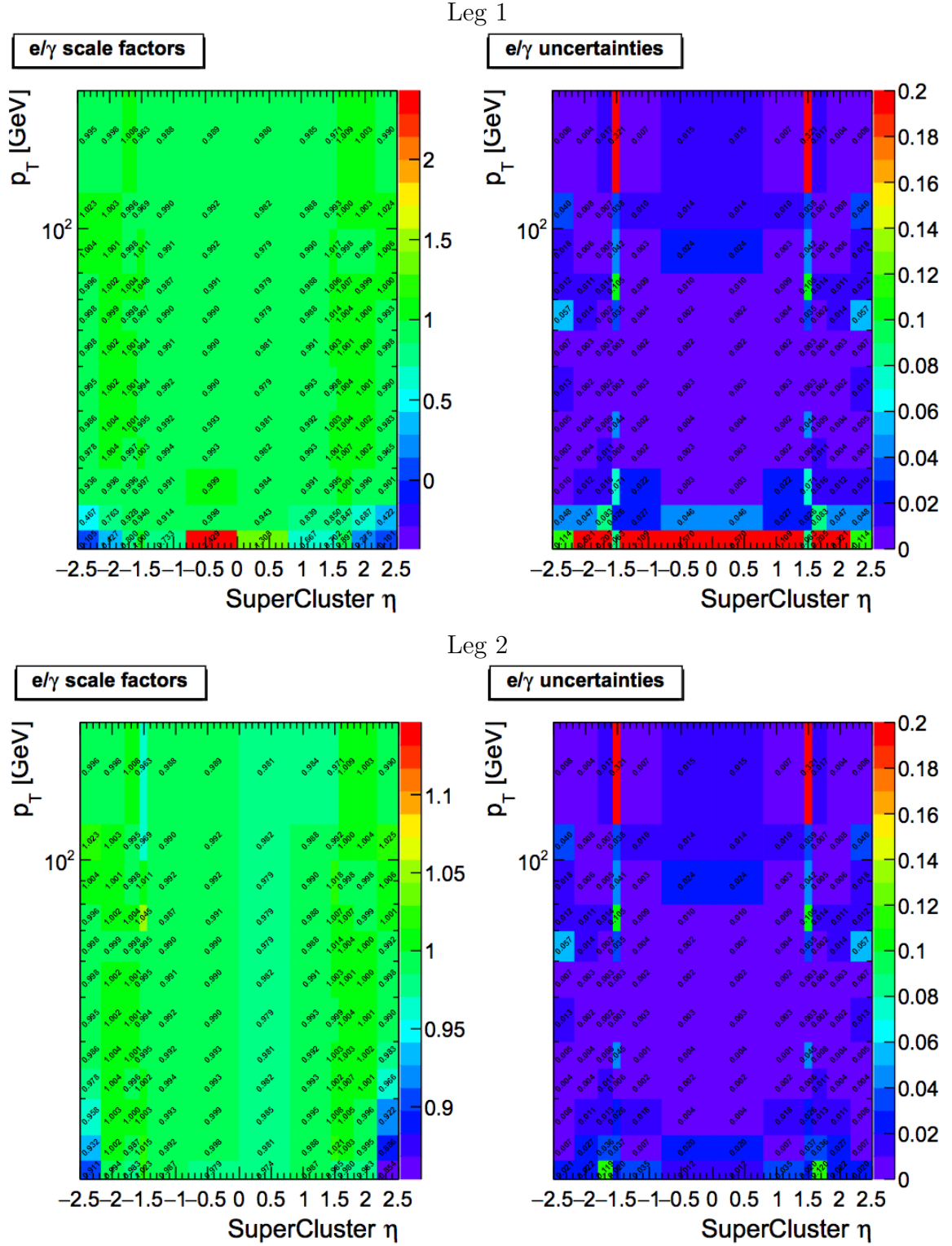


Figure 1.1: HLT trigger SFs for electrons approved by the CMS e/γ POG group. SFs are derived for both legs separately: Leg 1 (top) corresponds to the leading electron and Leg 2 (bottom) corresponds to the sub-leading electron. The values of the SFs are shown on the left, and the associated uncertainties with each value are shown on the right. Taken from [1].

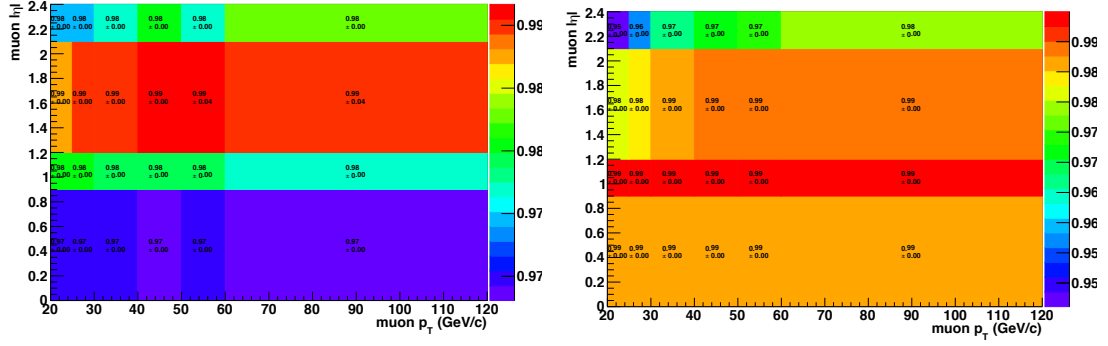


Figure 1.2: Final HLT SFs for muons as a function of p_T and η , measured for eras B to G. Left: Scale factors for 8 GeV leg (sub-leading muon). Right: Scale factors for 17 GeV leg (leading muons), provided that the sub-leading muon already passed 8 GeV p_T requirement.

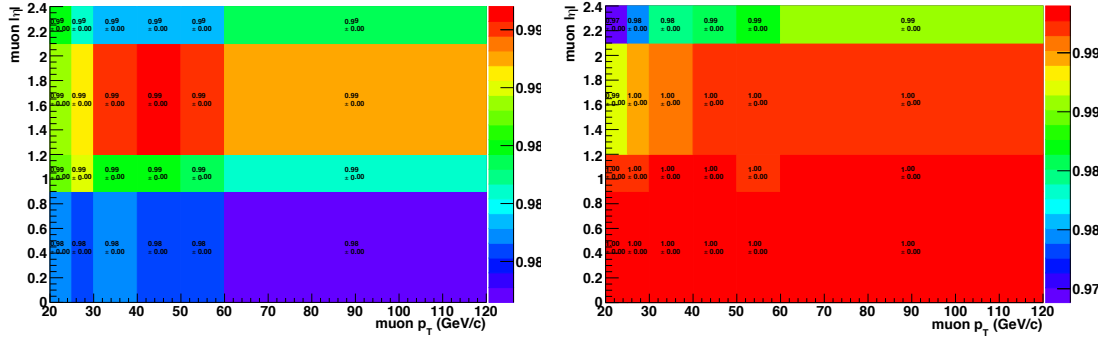


Figure 1.3: Final HLT SFs for muons as a function of p_T and η , measured for the era H. Left: Scale factors for 8 GeV leg (sub-leading muon). Right: Scale factors for 17 GeV leg (leading muons), provided that the sub-leading muon already passed 8 GeV p_T requirement.

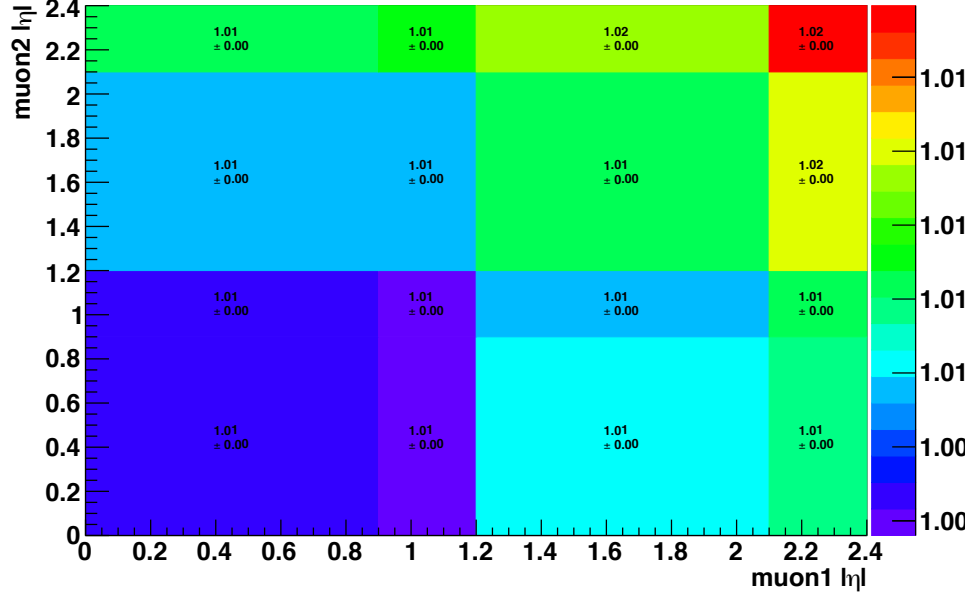


Figure 1.4: SFs for muons of the dZ requirement as a function of η 's of both muons.

1.4 Simulated Samples

The data analysis carried out in this thesis is optimised using the MC simulation. MC samples for signal and background processes have been produced with various HEP software (“generators”) that generates the processes of interest: processes that mimic the final state of this measurement.

1.4.1 Signal processes simulation

The signal Monte Carlo (MC) samples have been generated using MADGRAPH5_aMC@NLO [87] package. In these samples, simulated at leading order (LO), gluon fusion production of WED spin-0 and spin-2 narrow resonances is followed by the decay of the resonances to double Higgs boson system. All Higgs boson are assumed to be SM Higgs bosons with the invariant mass of 125 GeV. Samples are generated for two spin hypotheses and 16 mass values covering the range of heavy resonance masses

from 250 to 1000 GeV. Two types of signal samples are present: resonance decaying to $2b2l2\nu$ final state through the $X \rightarrow HH \rightarrow bbZZ$ decays and also through the $X \rightarrow HH \rightarrow bbWW$ decays. In both samples the first Higgs boson decays to a pair of b quarks. However, in the first sample the other Higgs boson decays to ZZ pair, while in the second sample the other Higgs boson decays to WW pair. Only Z boson decays in the a dielectron, a dimuon, or a two neutrino state are selected. For W bosons, the chosen signature is characterised by a W boson decay to an electron and an anti-electron neutrino or a muon accompanied by an anti-muon neutrino.

To compare the expected numbers of events in the simulation to the number of observed events in the data for a given integrated luminosity, the signal production cross section has been normalised to 2 pb. This is a typical value of the production cross section of the WED particle in the 250-300 GeV range, the range to which the current physics analyses are very sensitive with the available LHC data. Additionally, the computed event rates take into account the branching fractions of the corresponding di-Higgs decay chains to the final state: 0.0012 and 0.0266 for $HH \rightarrow bbZZ \rightarrow bbl\ell\nu\nu$ and $HH \rightarrow bbWW \rightarrow bbl\nu\ell\nu$, respectively [103].

1.4.2 Background processes simulation

In this analysis the main background processes are top-antitop production ($t\bar{t}$) and Drell-Yan production in association with jets. Other background processes that contribute to a lesser degree include the single top production, diboson production, and the production of a single Higgs boson in association with a Z boson (“ZH production”), see Table 1.2. Other background processes are fully rejected in the event selection and thus are neglected.

Table 1.2: Background Monte Carlo samples

DY plus 1 Jet	MADGRAPH5_aMC@NLO-PYTHIA
DY plus 2 Jets	MADGRAPH5_aMC@NLO-PYTHIA
DY plus 3 Jets	MADGRAPH5_aMC@NLO-PYTHIA
DY plus 4 Jets	MADGRAPH5_aMC@NLO-PYTHIA
WW	PYTHIA
WZ	PYTHIA
ZZ	PYTHIA
ZH with $H \rightarrow b\bar{b}$ and $Z \rightarrow \ell\ell$	MADGRAPH5_aMC@NLO
$t\bar{t}$	POWHEG-PYTHIA
top quark tW channel	POWHEG-PYTHIA
\bar{t} quark tW channel	POWHEG-PYTHIA
top quark t-channel	POWHEG-PYTHIA
\bar{t} t-channel	POWHEG-PYTHIA
top quark s-channel	MADGRAPH5_aMC@NLO-PYTHIA

Drell-Yan (DY) process in association with one to four jets is generated at leading order (LO) using MADGRAPH5_aMC@NLO with the MLM matching scheme [110]. To account for the higher order QCD and electroweak effects in V+jets production (following [?]), DY events are further reweighted according to the dilepton transverse momentum.

The simulations of the background processes associated with top quark production are generated at next-to-leading order (NLO). POWHEG [?, ?, ?, 158] generator was used to generate the samples for top quark pair production and single top quark production in the tW and t channels. For the single top s channel production, the MADGRAPH5_aMC@NLO generator was used. Single top backgrounds have been rescaled to the theoretical values of the NNLO cross sections [?, ?].

PYTHIA 8.212 [?, 156] was used to generate diboson samples at LO. Diboson background yields are normalized to NLO cross sections [?, ?, ?]. The dominant SM Higgs background process, the SM production of a single Higgs boson in the association with a Z boson (ZH), is simulated at NLO using the MADGRAPH5_aMC@NLO gen-

erator with FxFx merging [157]. The SM Higgs background from the ZH process is scaled to NNLO with the MCFM program [112]. All the final cross section values at the NNLO accuracy in perturbative QCD have been computed with the original generators and are found to be in agreement with the values from the LHC Higgs cross section working group [97, 99–102].

Normalizations for $t\bar{t}$ and DY background processes are determined from data, as explained later in this chapter. The NNPDF3.0 [?] parton distribution functions (PDF) set is used for all the LO and NLO samples. POWHEG and MADGRAPH5_aMC@NLO interfaced with PYTHIA8.212 are used for the parton showering and hadronization stages. The description of the underlying event is done using the tune CUETP8M1 derived in [155]. For the simulation of the CMS detector response, GEANT4 [92] was used. For all MC simulations, further reweighting of events is done using the SFs derived to account for the discrepancies between the data and simulation: lepton identification and b tagging efficiencies, see Section ?? . As discussed in the Section ?? , multiple overlapping proton-proton interactions occurred in each bunch crossing during data collecting in 2016, with an average of 24 hard scattering vertices per event. To account for this fact, all simulated samples include additional interactions to reproduce the real pileup distribution measured in data.

1.5 Physics Objects Selection

During the reconstruction of the collisions at the CMS, data for each event are refined into high-level physics objects that correspond to particles created as a result of the proton-proton interaction. Among the physics objects necessary for this measurements are reconstructed electrons, muons, jets originating from quarks of heavy flavor (b jets), and the missing transverse momentum. The reconstruction details

have been given in Section ??, here we focus on the analysis specific selection of each of these physics objects.

1.5.1 Electrons

Electrons are reconstructed using the GSF algorithm [74]. The electron candidates are then selected by first applying a loose isolation requirement of 0.4, after which they have to pass Tight ID criteri defined by the CMS e/γ POG, see ??. At the offline level, the analysis applies additionally the loose WP (WP90) [1]. With this WP, utilising variables such as the agreement between the position of the ECAL cluster and GSF track that form the electron, the energy of the 3 by 3 crystal core of the electron's cluster, the ratio of the electron energy measured in ECAL to electron's momentum measured in the tracking system, etc., one achieves an electron selection efficiency of 90%. This is a justified level of the desired identification efficiency for the $Z \rightarrow \ell\ell$ channel since we select on-shell Z boson decays to charged leptons, where produced prompt leptons are very energetic. Finally, the electrons are required to be isolated from other particles in the event. Numerically, a selection criterion on the isolation ?? is imposed, where the expected contribution of particles from pileup interactions is ρ -subtracted using the effective areas method, see Section ??. In this measurement, the isolation (with the cone size 0.3) for electrons is required to be smaller than 0.06, which means that all other particles together in the isolation cone around the electron cannot have more than 6% of the electron's energy.

1.5.2 Muons

Muon candidates are reconstructed using tracker muon and global muon tracks identified by the PF algorithm. The selection procedure is similar to the one of electrons:

first a loose relative isolation selection of 0.4 is applied, then muons have to pass the Tight WP of the muon ID selection. At the offline level, a more stringent set of quality requirements (WP Loose) recommended by the CMS Muon POG is applied to the muon object. Lastly, a relative $\Delta\beta$ -subtracted PF isolation selection of 0.15 is applied, with the cone size 0.4.

1.5.3 Jets

Jets are reconstructed using the anti- k_T jet clustering algorithm. This algorithm clusters PF candidates in a cone of the radius 0.4. The energy and the resolution of the produced jets (so-called AK4 jets) are further corrected using JEC and JER corrections. These are used to calibrate the energy of the jets and to smear the resolution of jets to match the one in the data.

To reject misreconstructed jets due to detector noise, pileup, etc., a loose jet identification WP is applied following the recommendations from the CMS JetMET POG. If jets are found to be overlapping with charged leptons used in the measurement, these jets are not considered by the analysis. We consider jets with a p_T greater than 30 GeV, which are in the range of $|\eta| < 2.4$. At least two jets must be present in the event.

1.5.4 b jets

Each identified jet is further assigned a probability to originate from the b quark using the CMVA b tagging discriminator. These tagger as an output produces a continuous discriminator, a value between -1 and 1, that is used to define three WPs depending on the chosen discriminant value. CMS BTag POG provides the CMS with the WP Loose, Medium, and Tight. For our measurement, the WP Medium

requirement (>0.4432) is found to lead to the best expected (from the simulation) results. Therefore, the WP Medium is chosen in this analysis for the derivation of the final results. Jets passing the WP Medium requirement are classified as b jets. The threshold is chosen such that the misidentification rate for light-quark and gluon jets is about 1% and the b jet tagging efficiency for this working point is about 66%. Two b jets with the largest scores of the CMVA discriminator are used to reconstruct $H \rightarrow b\bar{b}$ candidate, which will be explained at length later in this chapter.

1.5.5 Missing transverse momentum

In this measurement two neutrinos are present in the final state, they come from the off-shell Z boson decays to neutrinos and also from leptonic decays of W bosons. Even though the two neutrinos present in the signal events cannot be identified directly by the CMS detector, their presence can be inferred from the combined transverse momentum vector, using the momentum conservation requirement in the transverse plane for each event. The missing transverse momentum \cancel{p}_T is computed as the negative vector sum of the transverse momenta of all visible PF objects and is further JEC and JER corrected, see Section ???. The missing transverse energy \cancel{E}_T is the magnitude of the \cancel{p}_T vector.

All corrections recommended by the CMS JetMET POG are applied [162]. Additionally, a set of filters related to the instrumental effects is employed, such as removal of the misreconstructed signal in the HCAL, noise in the tracker, etc. [163].

1.6 Event Selection

The candidate events are selected in the data sample if they contain the following physics objects: 2 b jets, 2 charged leptons, and a missing transverse energy. Then

we reconstruct intermediate particles of the decay chain by combining the observed physics objects: $Z \rightarrow ll$ and $Z \rightarrow \nu\nu$ are reconstructed first. Then $H \rightarrow ZZ^*$ and $H \rightarrow b\bar{b}$ are reconstructed. Finally, two Higgs boson candidate are used to form the HH system that could originate from a narrow resonance we are searching for.

In this chapter we discuss how HH candidates are formed, how the selection criteria is applied to reduce contamination from background processes in signal-enriched region, how kinematic quantities used to compute the final results are defined, and how well simulation represents the data.

1.6.1 Kinematic selection of physics objects

We have described the kinematic selection of leptons and jets (and b jets) in the previous chapter. Because there is another $bbZZ$ measurement in the CMS Higgs group, our analysis shares some phase space with the other measurement. Therefore, the results may contain certain overlap. The other $bbZZ$ team studies the $2b2l2q$ final state, where q stands for any quark initiating the jet. To ensure that both measurements produce statistically independent (“orthogonal”) results, the selection on the MET is introduced. Since the final results - the production cross sections times the BF’s of the final state - depend on the mass point, the MET selection varies with mass. While the derivation of the final results (called “limits”) will be explained later in this chapter, at this point, it is worth to point out that both analyses computed limits for all resonance mass hypotheses applying different MET selection criteria, see Fig. ???. The found set of MET requirements that yielded the best combined limits (see Table 1.3), when the results of two measurements are merged together, is used by both teams.

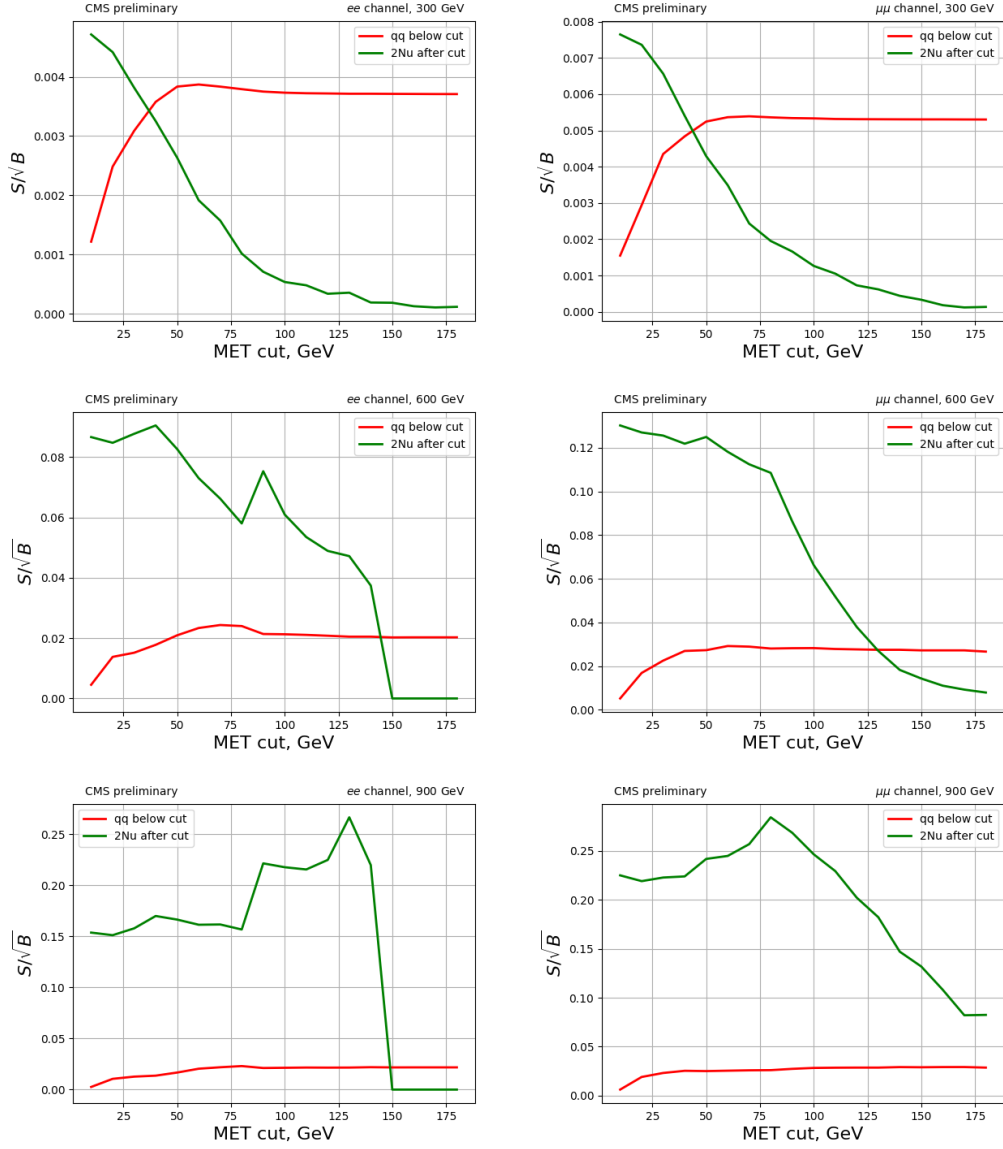


Figure 1.5: Optimisation of the MET selection for two $bbZZ$ analyses. S and B stand for signal and background process' yields respectively. Significance-like figure of merit (\sqrt{S}/B) as a function of the MET cut is used to identify the best selection for each given mass hypothesis. Green curve shows the significance for this measurement, where events are kept above a given threshold. Red curve shows the significance for the other $bbZZ$ measurement, where the MET requirement is inverted (events are kept below that threshold). Top: 300 GeV mass. Middle: 600 GeV mass. Bottom: 900 GeV mass. On the left di-electron channel, di-muon channel is shown on the right.

Table 1.3: The MET requirements as a function of the mass of the HH candidate. Selection values (the second column) are provided for different mass hypotheses (the first column) of the narrow resonance decaying to the HH system.

Signal mass, GeV	\cancel{E}_T selection, GeV
260-300	> 40
350-600	> 75
650-1000	> 100

1.6.2 Signal candidate construction and selection

Two leptons of opposite sign and same flavor with the invariant mass higher than 76 GeV are selected as Z candidates. This mass requirement helps rejecting di-lepton candidates not corresponding to real Z bosons. Events with di-lepton mass higher than 76 GeV will be used for SR and $t\bar{t}$ CR. Additional Z mass selection will be discussed in the corresponding section later in this chapter. These on-shell Z bosons are assumed to come from the $H \rightarrow ZZ^*$ decays. The other Z boson, off-shell Z boson, decays to two neutrinos in our signature, and is represented by MET. Lorentz four-vectors of the di-lepton candidate and MET are added and the resulting four-vector represents the first Higgs boson candidate.

The other Higgs boson is formed from the pair of b jets with the highest output value of the CMVA algorithm. No requirement is applied on existence or absence of other b jets in an event because such may be present due to a b jet misidentification or b jets resulting from pileup interactions or an underlying event. The invariant mass of the $H \rightarrow b\bar{b}$ candidate is required to be greater than 20 GeV to remove contamination from background events with low mass resonances that decay to two jets, such as events with J/psi, Upsilon or low energy QCD interactions. There is no upper requirement on the $H \rightarrow b\bar{b}$ invariant mass. Together with the first Higgs boson, the constructed di-Higgs system approximates the double Higgs boson

production that this measurement studies.

The final double Higgs boson candidate (HH candidate) comprises the $Z(\ell\ell)$ candidate, the MET representing the $Z(\nu\nu)$ decay, and the $H \rightarrow b\bar{b}$ candidate. The four-momentum of this HH candidate is defined as the sum of the four momenta of the two leptons and two b jets in the candidate as well as the four momentum of the MET, defined in Sec. ??.

HH system decays to a pair of b quarks and a pair of W bosons can also result in the same final state. The expected yields for the $bbWW$ channel with respect to the $bbZZ$ yields are comparatively small (1 to 4), because of the stringent kinematic selection on the di-lepton invariant mass. However, the contribution from the HH system decaying through the $bbWW$ intermediate state is still considered to be part of our signal in this measurement. The minimum requirement on the di-lepton mass is necessary to ensure that our measurement is orthogonal to the known HH search from CMS in the $bbVV$ channel that focused on $bbWW$ decays [123], where only events with the di-lepton mass below 76 GeV were studied.

In collider physics, one of several common definitions of the transverse mass is given by: $M_T = \sqrt{(E^2 - p_z^2)}$. This quantity is widely used in the CMS searches for new particles. We proceed in the same fashion constructing our final variable - $\tilde{M}_T(\text{HH})$, using the di-Higgs four-vector defined in the previous paragraphs.

While up until this moment we had the same requirements for the search of the $\text{radion/graviton} \rightarrow HH$ for any heavy resonance mass, it is worth noting that at this point the analysis becomes mass point-specific. This is because the selection on the BDT discriminant (explained later) and the MET requirement differ with the mass hypothesis. When we compute limits for different radion or graviton hypotheses, we apply different selection criteria.

Finally, the reader should be informed that if an event does not have enough

physics objects suitable (as discussed in the objects selection section) for building the $Z(\ell\ell)$ or $H \rightarrow b\bar{b}$ candidates, or if the event does not pass candidate selection requirements on those objects or the full HH system, the event is discarded.

1.6.3 Signal and control kinematic regions

Three regions are defined: signal-enriched or signal region, and two CRs. The signal region is chosen such that the expected signal fraction is the largest there. Two control regions are defined such that they contain predominantly the background events with almost no signal. We define two CRs, one for each of the two main background sources: the CR for $t\bar{t}$ (CRTT) and the CR for Drell-Yan in association with jets (CRDY).

Two intermediate particles in the decay chain are nearly fully reconstructed, such as $H \rightarrow b\bar{b}$ and $Z(\ell\ell)$. The signal region is defined in the phase space of $H \rightarrow b\bar{b}$ and $Z(\ell\ell)$ events. This corresponds to an area determined by the mass of the Higgs boson (125 GeV) and the mass of the Z boson (91.2 GeV). To account for the detector smearing effects, the mass windows near the pole masses are defined such that we select events within the $H \rightarrow b\bar{b}$ mass range from 90 to 150 GeV and Z mass range from 76 to 106 GeV, see Fig. 1.6. In the CMS, these relatively standard mass windows are chosen taking into account the detector resolution effects on a two b jet system and a di-lepton (and the natural width for a Z boson) mass and contain approximately 95% of true Higgs and Z boson candidates. The proportion of signal events is further increased with respect to background events by applying an additional requirement, the MVA requirement, which will be explained in the next section.

CRs are defined inverting the SR selection. Drell-Yan plus jets (or “DY” later for brevity) background process contains a real Z boson, while the two jets are random

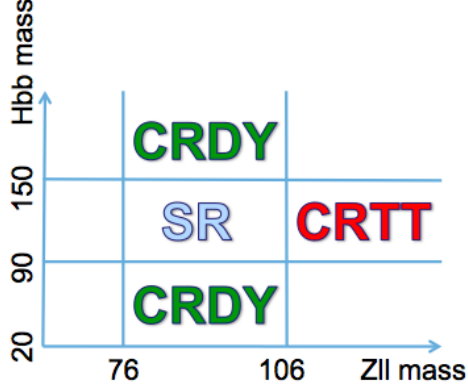


Figure 1.6: Signal region, control region $t\bar{t}$, and control region Drell-Yan in the phase space of $Z \rightarrow \ell\ell$ and $H \rightarrow b\bar{b}$ masses.

and have random invariant mass. We obtain the CRDY inverting the $H \rightarrow b\bar{b}$ selection. For CRTT, $t\bar{t}$ events always have two b quarks whose invariant mass has a broad distribution, while they do not have a real Z boson. Thus, to select CRTT, we invert the $Z(\ell\ell)$ selection and use only the events in the upper range of the Z mass, see Fig. 1.6.

CRs are used to fit the event yield of the simulated background processes to the event yield in data and, thus, to determine the relative normalisations of $t\bar{t}$ and Drell-Yan background processes, which is done using CRTT and CRDY correspondingly.

The efficiency of the candidate selection, up to this point, is summarised in the Table 1.4, where numbers are provided for the SR. The signal contributions are split into two components $bbZZ$ and $bbWW$, and are shown separately. The corresponding total numbers of events passing the selection are also given (the fourth column).

Table 1.4: Number of events surviving the candidate selection and kinematic requirements. Numbers are given for $bbZZ$ and $bbWW$ contributions in the SR. Efficiency values are also provided (the third column) and are normalised to the initial event counts before any selection is applied. Di-muon channel is presented. Numbers for di-electron channel have the same trend but lower values since in the CMS, efficiencies for electrons are lower than for muons.

Process	Mass, GeV	Efficiency, %	Number of events
bbWW	300	0.2	85
bbZZ	300	10.4	4511
bbWW	900	0.1	23
bbZZ	900	15.1	12963

1.6.4 Signal region candidate selection with a multivariate technique

After the SR and CRs have been defined, in the final step of the event selection we require the events in the SR to pass the threshold value of the BDT discriminant. An MVA discriminant that uses a boosted decision trees algorithm is trained considering a number of kinematic quantities of a candidate to be above a certain threshold. As this selection step is complex, it is described in a dedicated chapter: 1.7.

1.7 Multivariate selection in the signal region

To reduce the background contamination in the SR, we employ a standard practice of CMS physics analyses of utilising the MVA discriminant. In this section, we will discuss which discriminating variables were used, how the MVA discriminant was constructed, and what are the efficiencies of the BDT selection for all major signal and background processes.

1.7.1 Kinematic variables of a candidate

A number of kinematic quantities can be constructed out of four-vectors that comprise candidates of our final state. The distributions of these quantities in general differ for candidates originating from different background processes as opposed to for candidates from the hypothetical signal.

In this section we discuss a set of kinematic quantities that are the most discriminating between the expected signal candidates and background candidates. This set of variables is used as an input for computing the multivariate discriminate that is later discussed in this section. In total, nine variables are chosen for this purpose and discussed here. About 30-40 other kinematic variables were considered at early stages of this data analysis. However, they were discarded as it was found that they do not improve the results of this measurement in a significant way, while they increase considerably the complexity of the measurement.

Since the MVA selection requirement will be applied on a quantity computed based on these variables, the simulation has to reproduce the main variables well. We will define each of the nine variables below. For SR and both CRs, we will show the comparison of distributions from data and simulation for each variable. Since the number of plots would be too large to show for two channels and two spin hypotheses, not to mention for all masses, we will include in this dissertation only di-muon channel plots for 300 GeV graviton mass hypothesis. However, all other relevant figures of the nine main variables, including the di-electron channel and other mass points, were examined and discussed with CMS collaborators during the review of the measurement in CMS. They show a similar behaviour and agreement as those included here.

As we outlined before, even for simple physics objects the distributions from MC

simulations and data have discrepancies. For more complex objects and candidates, these discrepancies become even larger. In general, MC simulations are not supposed to reproduce well very narrow regions of the kinematic phase space or align with the data perfectly at the high order in the QCD. Therefore, one normally adjusts the rates of background processes using the normalisation values determined in the fit to data in the control regions. The distributions as they are, without the extra normalisations (from the fit) applied to the event yields of MC simulated background processes, are in general called pre-fit distributions. After the normalisations from the fit are applied on the rates of background processes, post-fit distributions are obtained.

The list below summarises the set of variables used as input to the MVA discriminant:

- **ΔR separation between two b jets.** The ΔR (defined in the Section ??) separation between the b jets ($\Delta R_{b \text{ jets}}$) gradually decreases as we start considering larger graviton or radion masses. This fact is explained by the Lorentz boost of the $H \rightarrow b\bar{b}$ system. When the heavy resonance produces two SM Higgs bosons, they are highly boosted. For the Higgs boson, which will further decay to a pair of b quarks ($H \rightarrow b\bar{b}$), the b quarks will come out of the decay almost collinear to each other with a minimal value of the $\Delta R_{b \text{ jets}}$. For background processes this separation does not depend on the graviton or radion mass hypothesis.
- **ΔR separation between two leptons.** The distance between two leptons in the $\eta - \varphi$ space ($\Delta R_{leptons}$) tends to be smaller for the di-lepton system coming from the real Z bosons originated from the $H \rightarrow ZZ$ decays, in comparison to the $\Delta R_{leptons}$ distance between two random OSSF leptons produced by background processes.

- **Missing transverse momentum.** \cancel{p}_T distribution coming from the off-shell Z bosons is constrained by the invariant mass of the parent Higgs boson and has, thus, a more narrow distribution. Contrary, the MET coming from $t\bar{t}$ background process can produce smaller and larger values of the MET.
- **Invariant mass of the $H \rightarrow b\bar{b}$ candidate.** $H \rightarrow b\bar{b}$ mass for two b jets coming from real Higgs boson tends to be close to the SM Higgs boson invariant mass smeared by the b jet energy-momentum resolution, while the background candidates from unrelated b jets can have smaller and larger masses, especially if they come from the top quarks of the $t\bar{t}$ background.
- **Transverse momentum of the $H \rightarrow b\bar{b}$ candidate.** The transverse momentum of the $H \rightarrow b\bar{b}$ candidate ($p_T^{Hb\bar{b}}$) tends to be have a relatively narrow peaky distribution for candidates coming from the hypothetical signal in comparison to broad distributions produced by the background processes.
- **Invariant mass of the ZZ^* system.** ZZ^* mass of two Z bosons coming from the Higgs boson decay ($H \rightarrow ZZ$) tends to be close to the SM Higgs boson mass smeared by the \cancel{p}_T resolution, while the background candidates from DY production in association with jets can have random masses, which can be particularly large if they come from the DY production in association with several jets in addition to some instrumental MET present in the event.
- **Transverse momentum of the ZZ^* system.** The transverse momentum of the $H \rightarrow ZZ$ candidate (p_T^{Hzz}) tends to be have a relatively narrow peaky distribution for candidates coming from the hypothetical signal in comparison to broad distributions produced by the background processes.

- **Invariant mass of the Z boson candidate.** Z bosons coming from the Higgs boson have the invariant mass near the pole mass, while Z bosons from DY plus jets production can have a broader peak.
- **Transverse momentum of the Z boson candidate.** The transverse momentum of the Z candidate (p_T^Z) tends to be have a relatively narrow distribution for candidates coming from the real Z boson produced in the decays of the hypothetical signal in comparison to broad distributions of the $p_T^{\ell\ell}$, when di-lepton systems are produced by background processes.

At this stage of the analysis description, we would like to refer the reader to the pre-fit plots (figures in the left columns). The figures are shown in the following order: all nine distributions in CRDY ??, in SR ??, and in CRTT ??. The simulated distributions are found in an acceptable agreement with those from the data and are judged to be adequate for a use in a multivariate discriminant construction discussed next.

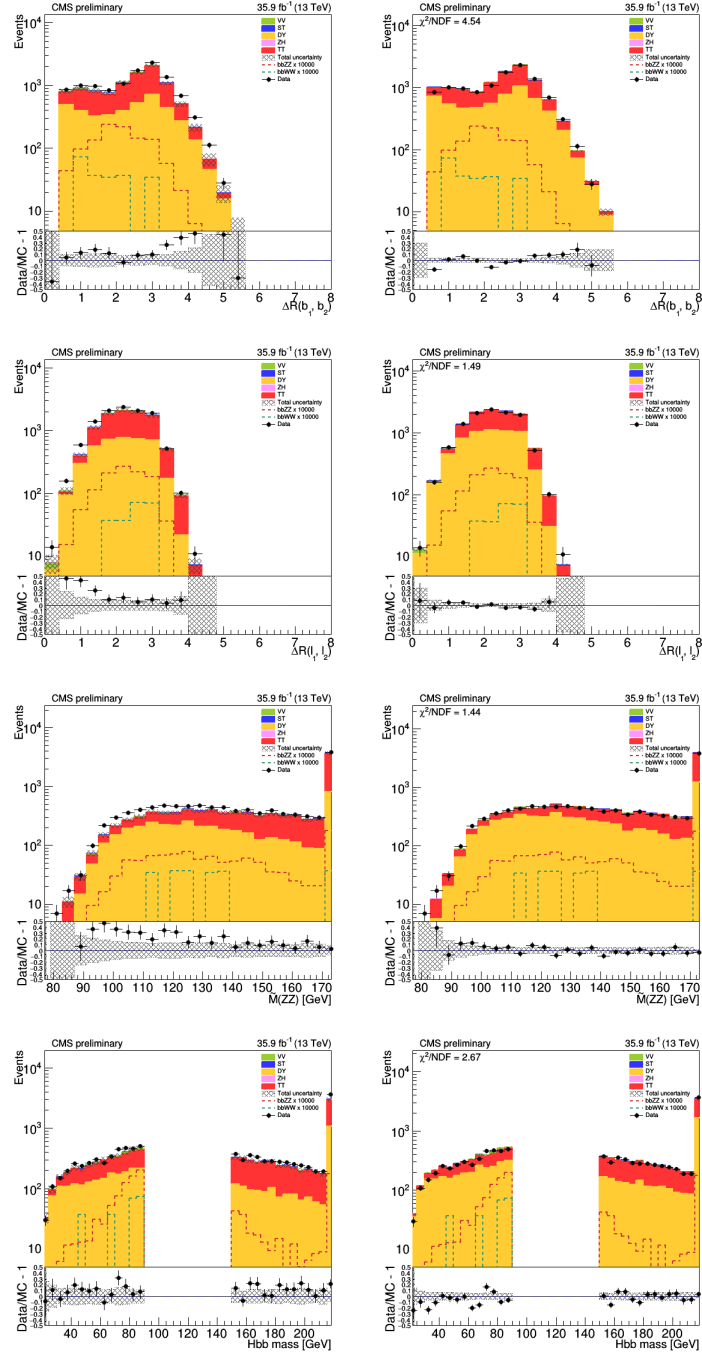


Figure 1.7: Comparison of data and MC samples. 300 GeV, CRDY region, mm channel. Prefit plot on the left, Full Postfit plot on the right.

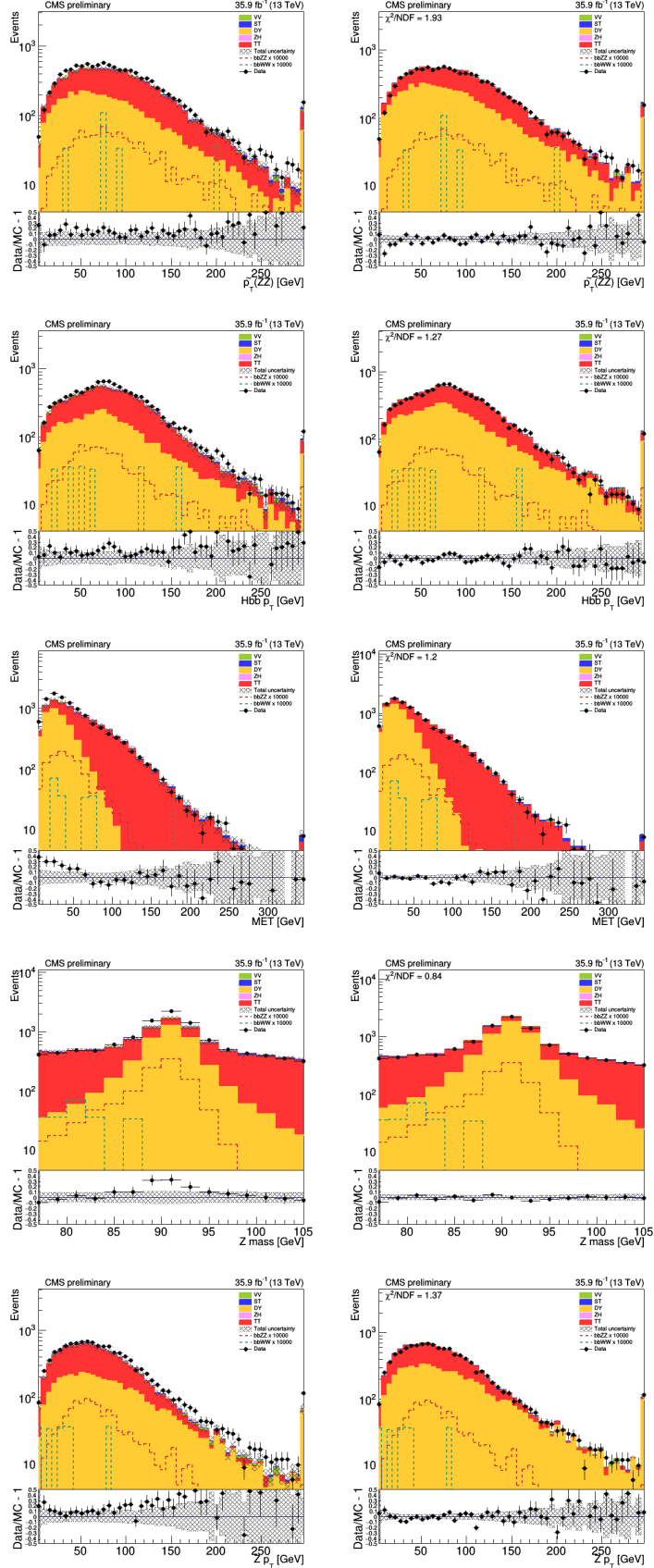


Figure 1.8: Comparison of data and MC samples. 300 GeV, CRDY region, mm channel. Prefit plot on the left, Full Postfit plot on the right.

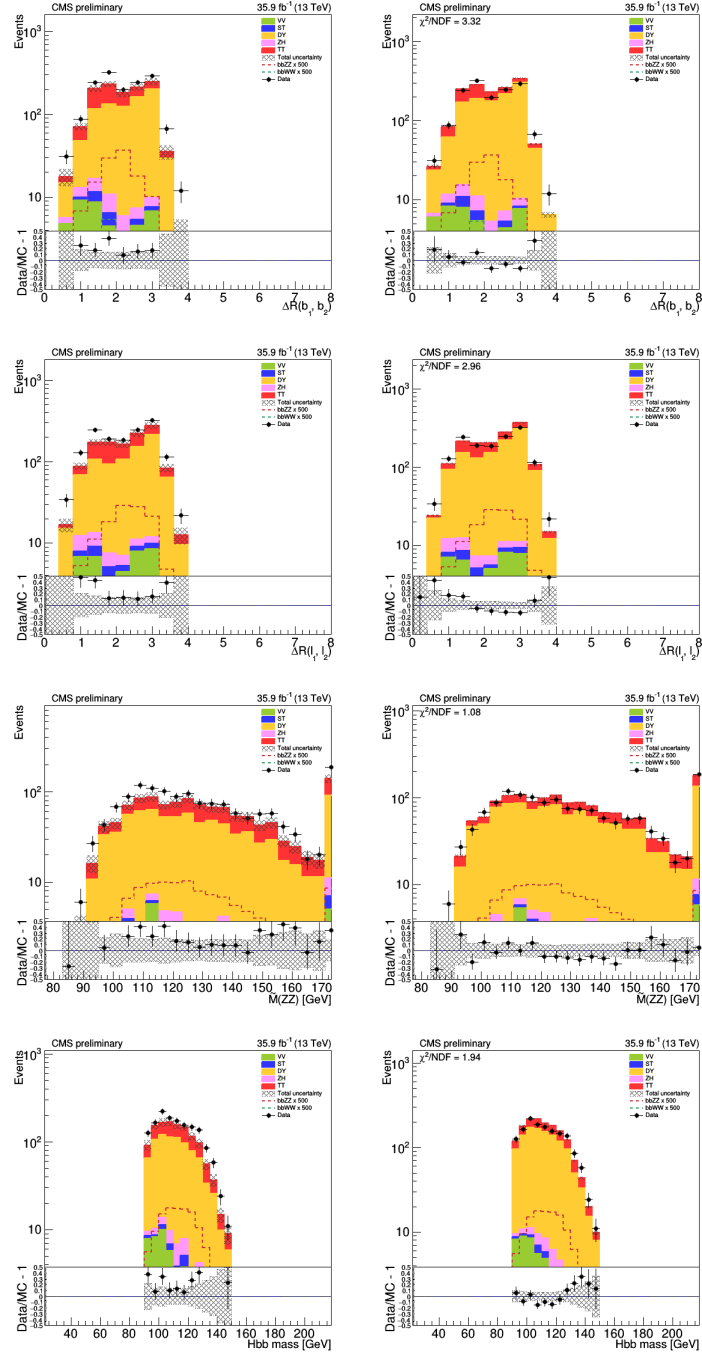


Figure 1.9: Comparison of data and MC samples. 300 GeV, SR region, mm channel. Profit plot on the left, Full Postfit plot on the right.

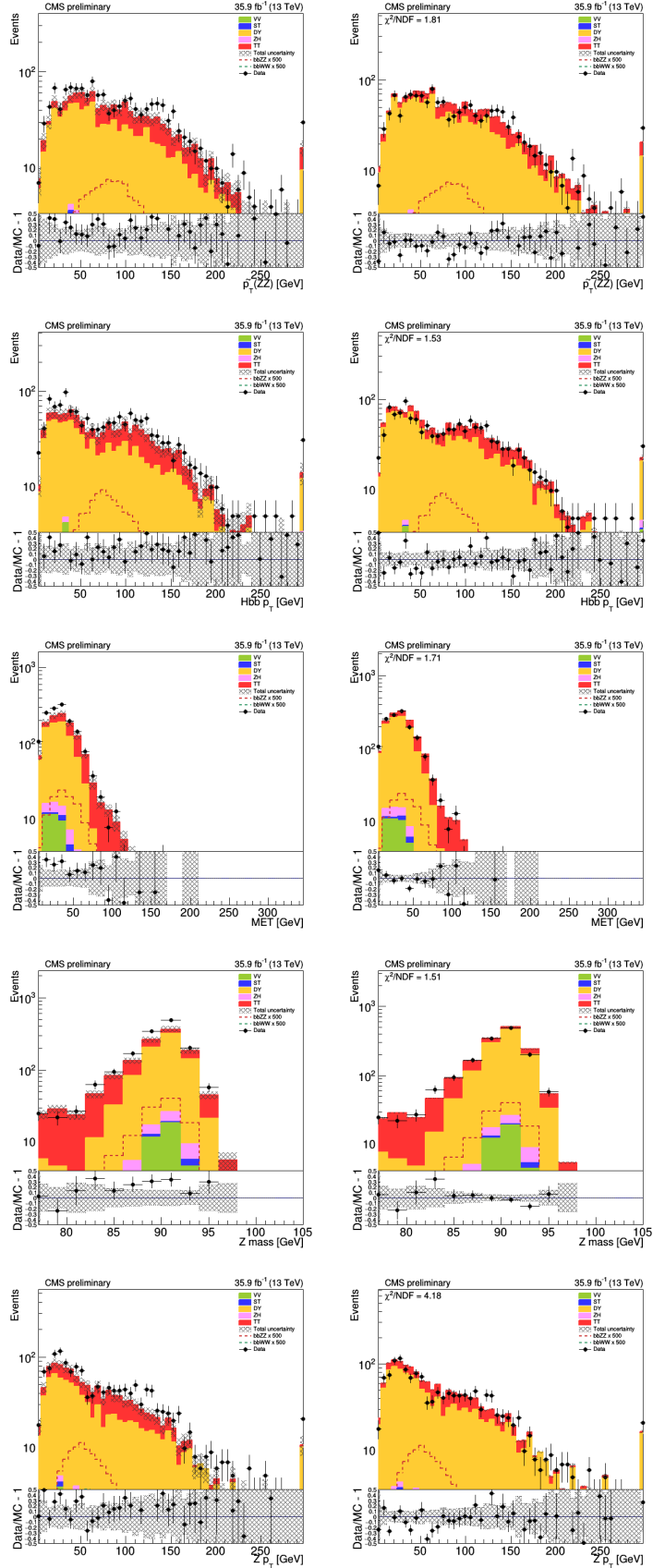


Figure 1.10: Comparison of data and MC samples. 300 GeV, SR region, mm channel. Profit plot on the left, Full Postfit plot on the right.

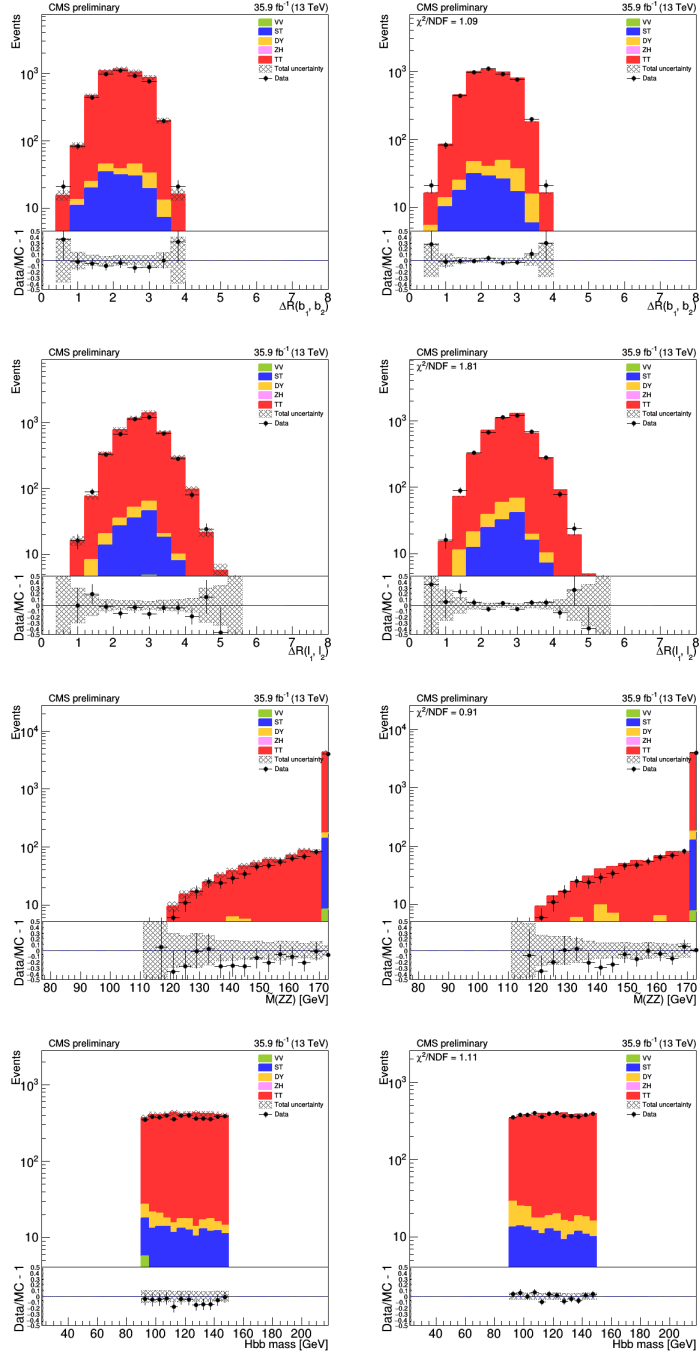


Figure 1.11: Comparison of data and MC samples. 300 GeV, CRTT region, mm channel. Profit plot on the left, Full Postfit plot on the right.

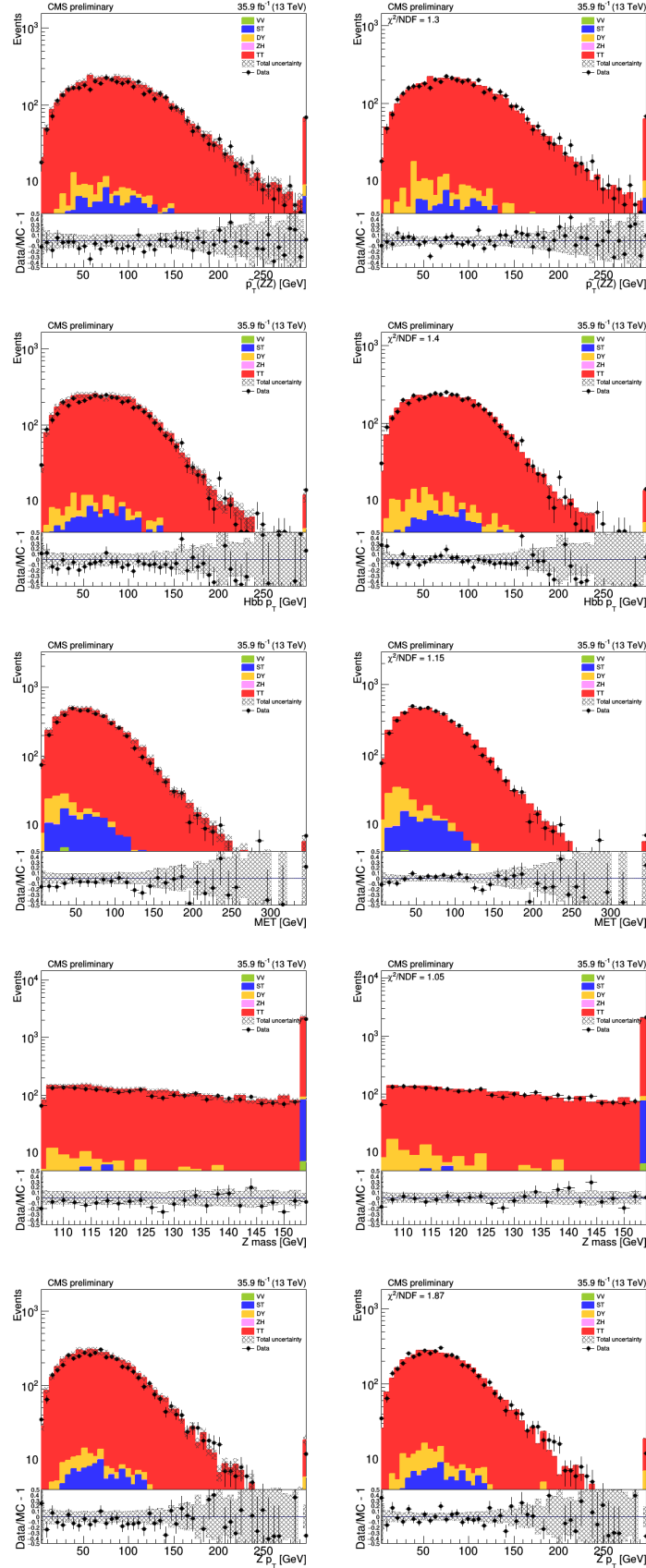


Figure 1.12: Comparison of data and MC samples. 300 GeV, CRTT region, mm channel. Prefit plot on the left, Full Postfit plot on the right.

1.7.2 Multivariate discriminant: a BDT classifier

In HEP in many areas, such as an object identification, a reduction of the background contribution in the signal region, etc., there are needs to discriminate a “signal” from one or several “backgrounds”. The discriminating algorithms can use a single physical variable for signal-background separation, or several variables. The way an algorithm uses the input variables can be of a sequential nature, or through some non-linear dependence. The Higgs boson discovery, in part, was possible due to an employed BDT approach, where several variables are combined into an artificial BDT score or output. The BDT output, as a higher-level construct, has no direct physical interpretation. However, due to the shown gain in signal-background separation performance, the BDT has been successfully used for years for the final classification decision.

Multivariate discriminants (or models or classifiers) based on the BDT or other algorithms are constructed using machine learning (ML) techniques. Now, almost at every stage of the HEP data analysis, starting from the track reconstruction, through the object identification and the signal region purification, up to the construction of the final discriminating MVA variable, physicists rely on the ML methods.

In simple terms, the ML procedure consists of the training and testing stages (sometimes also the validation stage is added). First, the data is split into two non-overlapping sets: a train and a test data. Then, the classifier is trained, when the model is learning the patterns in the train data. After that, the performance of the model is tested using the independent test data.

After the training procedure, ML algorithm produce a discriminator, which is a function that is related to the likelihood of an event to belong to a signal or to a background category. Here and in other parts of the thesis, we are describing the BDT procedure, which is a non-parametric supervised learning method used for

classification; other MVA methods that are not related to this measurement, are well-explained in [?].

Every analysts would always like to have a classifier that has a low bias and a low variance. A bias is a difference between the average prediction of our model and the correct value, which we are trying to predict. A classifier with a high bias oversimplifies the model and does not take into account all the nuances of a given train data. Therefore, one prefers a low bias models, which are flexible and perform well both on the train and test data, and always provide a stable good separation between the signal and background hypotheses. A variance is the variability of model prediction for a given data point. A variance is related to the spread of our data. A model with high variance learns almost every single pattern in the train data and, therefore, will not generalise well, when given new unseen data. As a result, models with a high variance achieve the best scores using the train data but perform poorly on the test data. Thus, one prefers a low variance models, which are robust when applying the trained classifiers on a dataset that is statistically independent from the one used for training.

One of the most popular ML algorithms in HEP is based on the boosted decision trees (BDT). A single decision tree is a sequence of simple binary splits on each of the input variables. The tree, thus, can be depicted as a multidimensional set of selections on input space. The tree assigns a score of +1 or -1 if a given event is signal or background-like. The key elements in each step of the BDT splits are the variables used for the selection and the positions of the selections. Both are determined using an impurity criterion $I(p_n)$, which is a function of the signal purity p_n in tree node n . The signal purity is defined as a ratio of the signal contribution to the total number of signal and background events, $p_n = S/(S + B)$. The impurity criterion is chosen such that it is at the minimum when $p_n=0$ or $p_n=1$. These values would give a

perfect signal-background discrimination. The criterion is at the maximum, when $p_n=0.5$, which means no discrimination is achieved. Each split maximises the gain function $G = I(p_n) - f_1 I(p_{c1}) - f_2 I(p_{c2})$. In this formulation of G , the labels $c1$ and $c2$ refer to child nodes of the parent node, and $f1$ and $f2$ are the fractions of events of the parent node that are found in child nodes $c1$ and $c2$, respectively. As a definition of the impurity criterion for this measurement, the Gini coefficient is used: $I_G(p_n) = p_n \cdot (1 - p_n)$.

The tree keeps applying the selection on the input variables until either a maximum depth is reached (a number of consecutive splits), or a minimum number of events in the final child nodes are attained. The problem with such a tree growing procedure is that it is prone to overtraining, which means the model will not generalise well and have a high variance. One way to deal with BDT overtraining is boosting. The idea behind boosting is, that signal events from the training sample that end up in a background node or vice versa, are given intentionally large weights (a penalty). These weights are normally significantly larger than the weights for events with the correct leaf node prediction. Such penalty procedure reweighs the train data and then new decision trees are created. The boosting is applied hundreds of times, which produces a set of new reweighed trees (a forest). Intuitively, the boosting is a method in which a large number of shallow trees, which have only a few splits, are combined by taking a weighted average of their output scores. The discriminating power of a single shallow tree is usually poor, but such a tree is less prone to overtraining, therefore, when combined, the ensemble of these trees produces a model with a high and stable performance.

For the boosting algorithm, we chose the gradient boosting method, as is implemented in the popular MVA package for HEP - TMVA [165]. Gradient boosting can be thought of as a function expansion approach. In this case each tree corresponds to

a summand. The parameters for each summand (tree) are determined by minimising of an error function. In the TMVA implementation, the binomial log-likelihood loss function is used. The adopted procedure follows the greedy algorithm approach - only one tree is modified at a time, while the other trees remain invariable.

Several decision trees of the BDT procedure, that is employed in the analysis, are shown below. This training was done in the d-electron channel. In all figures produced by the TMVA, the index 0 refers to $H \rightarrow ZZ$ candidate and index 1 refers to $H \rightarrow b\bar{b}$ candidate. For example, “hmass1” denotes the mass of the $H \rightarrow ZZ$ candidate, “hpt0” denotes the p_T of the $H \rightarrow b\bar{b}$ candidate, etc. For the Z boson candidate, the on-shell Z boson decaying to charged leptons, $Z(\ell\ell)$, has either an index 0 or the index is dropped. The closer the node color is to blue, the more the event is classified as signal-like, same idea is illustrated with the red color for background events.

Di-electron and di-muon channels have been trained separately and the BDT metrics (discussed later in this chapter) show similar performance. That is why to save the space, in this chapter we show mostly figures related to the di-electron channel.

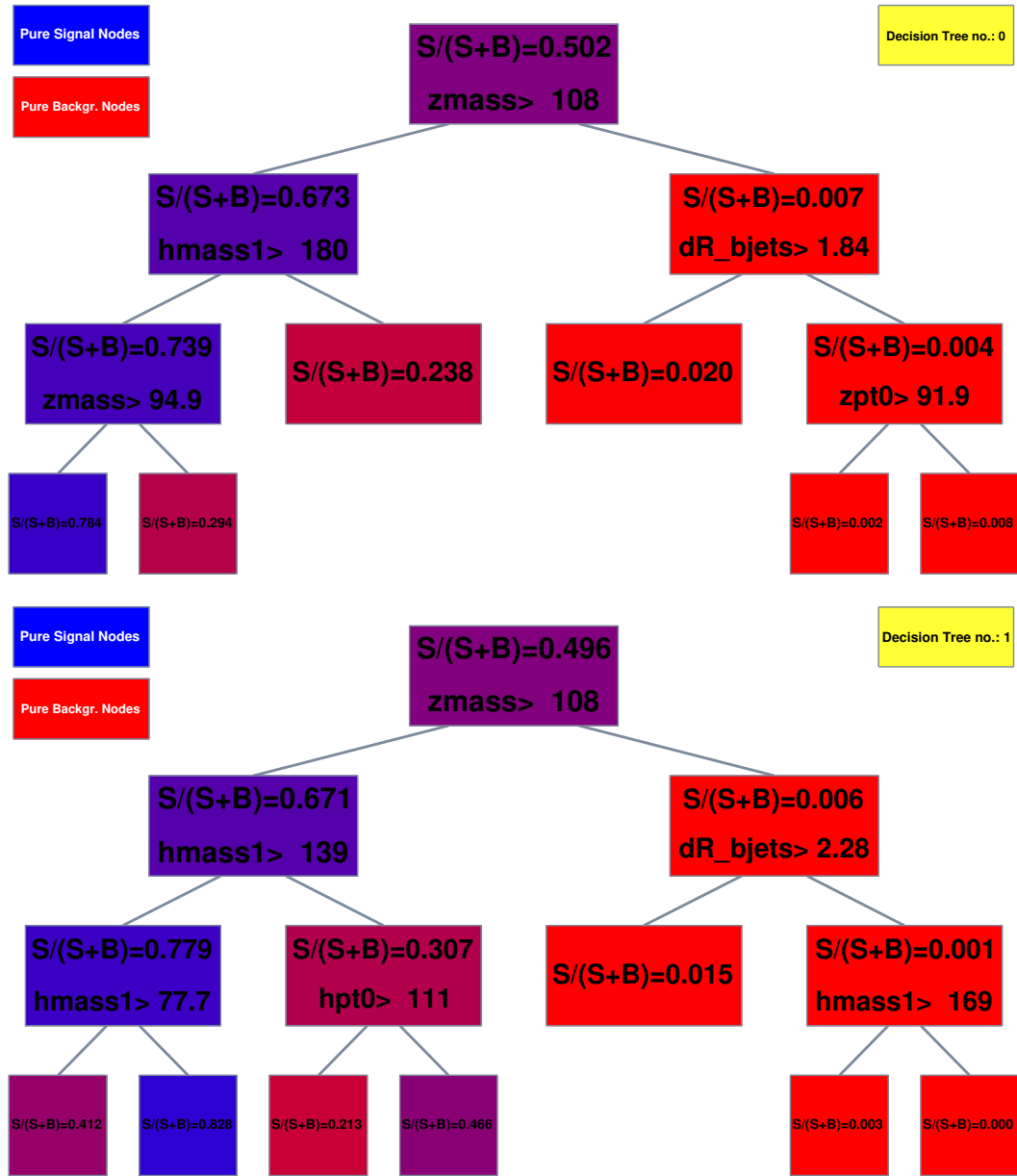


Figure 1.13: BDT trees 1 and 2 (indexing starts from 0). These trees relied on: the mass and the p_T of the $Z(\ell\ell)$ candidate, ΔR separation between two b jets, the mass of the $H \rightarrow b\bar{b}$ candidate, and the p_T of the ZZ^* system. The TMVA notation is explained in 1.7.2.

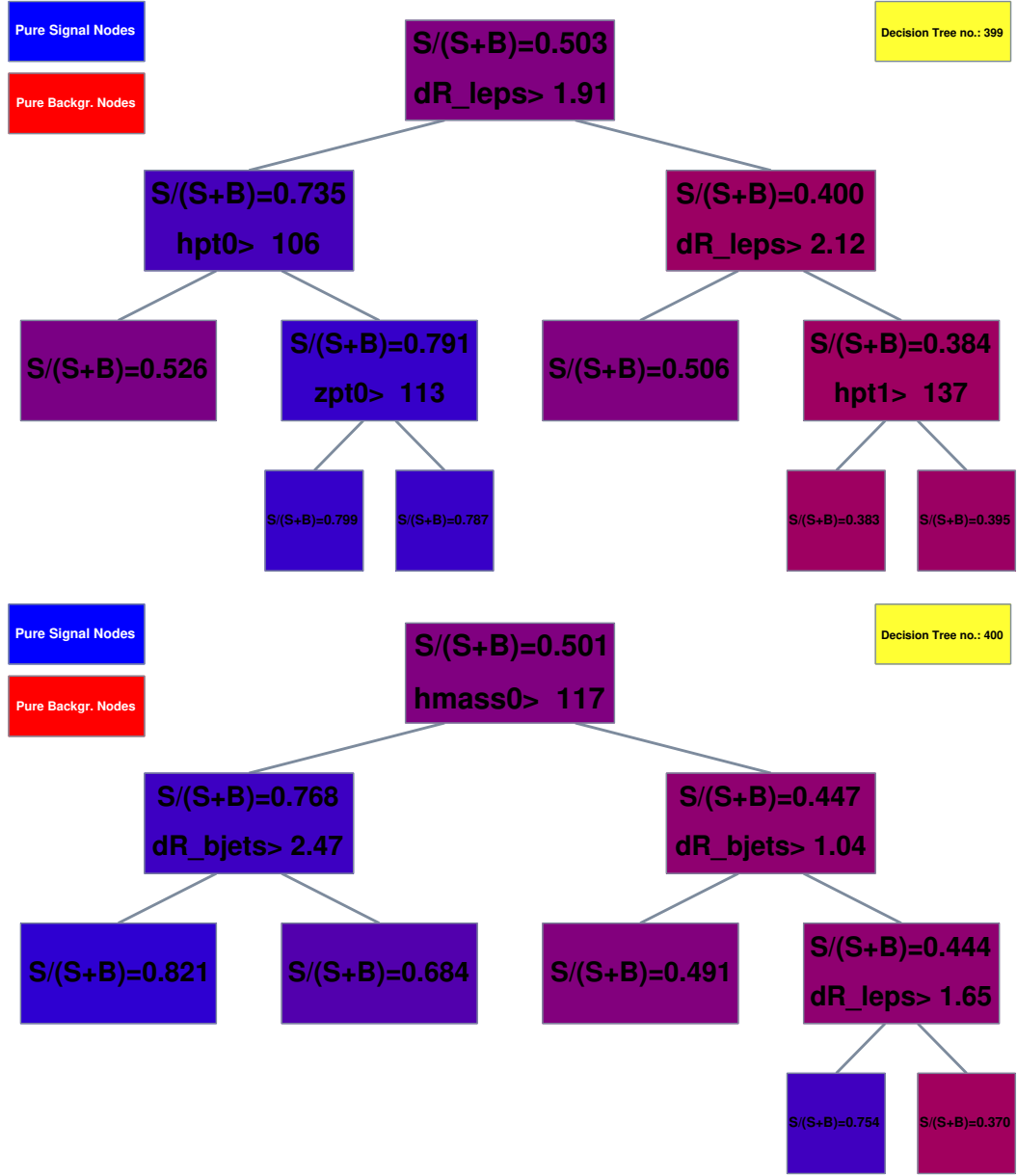


Figure 1.14: BDT trees 400 and 401 (indexing starts from 0). These trees relied on: the p_T of the $Z(\ell\ell)$ candidate, ΔR separation between two b jets, ΔR separation between two charged leptons, the p_T of the $H \rightarrow b\bar{b}$ candidate, and the mass and the p_T of the ZZ^* system. The TMVA notation is explained in 1.7.2.

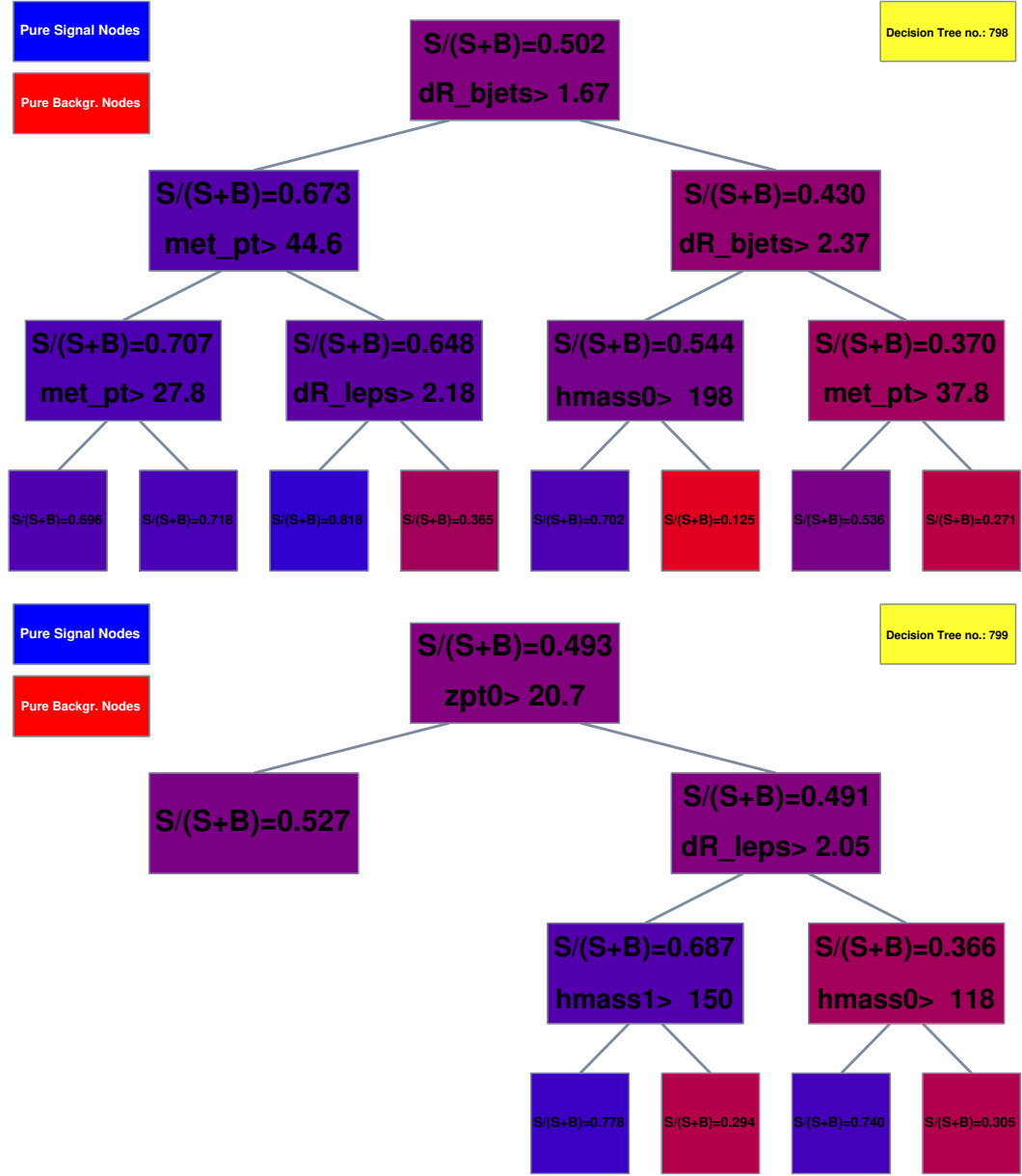


Figure 1.15: BDT trees 799 and 800 (indexing starts from 0). These trees relied on: the p_T of the $Z(\ell\ell)$ candidate, ΔR separation between two b jets, ΔR separation between two charged leptons, the mass of the $H \rightarrow b\bar{b}$ candidate, and the mass of the ZZ^* system. The TMVA notation is explained in 1.7.2.

The BDT discriminant (later the BDT for brevity) is trained on a pure sample of signal and background events from simulation, using the train data. The properties

of the discriminant are studied on an independent testing sample of pure signal and background events, using the test data. The Deep Neural Network (DL) approach also has been studied, however, due to the lack of the event statistics, the DL approach could not offer a performance higher than the one achieved with the BDT, and thus, was abandoned. Training 16 BDTs per the spin hypothesis seems unpractical since our data analysis is dominated by the statistical errors. Instead, we follow an approach of other HH analyses [?]: we split the range from 250 to 1000 into two regions: low mass (250 to 450 GeV) and high mass (500 to 1000 GeV) regions. This separation boundary at 450 GeV was optimised first using ROC curves (described later in this section), then running the whole analysis chain all the way to the final limits. This procedure not only saves CPU cycles, training two BDTs instead of sixteen, but mostly increases the statistics and improves the robustness of the trained BDT.

During the training procedure, some variables provide more discriminating power and on average are used more often than others. The more often the variable is used, the higher is its importance. The tables below show the ranking and average importance of each of the BDT training: low and high mass regions, di-electron and di-muon channels, see Tables ??.

Rank	Variable	Importance, %
1	$\Delta R_{b \text{ jets}}$	13.9
2	MET	12.1
3	Mass of $H \rightarrow b\bar{b}$ candidate	11.9
4	$p_T^{ZZ^*}$	11
5	$\Delta R_{leptons}$	10.9
6	p_T of $H \rightarrow b\bar{b}$ candidate	10.7
7	p_T of Z boson candidate	10.2
8	Mass of ZZ^* system	10.1
9	Mass of Z boson candidate	9.26

Table 1.5: Di-electron channel. Relative importance of the input variables in the low mass BDT training.

Rank	Variable	Importance, %
1	$\Delta R_{leptons}$	14.1
2	Mass of $H \rightarrow b\bar{b}$ candidate	13.7
3	$\Delta R_{b\ jets}$	13.2
4	p_T of $H \rightarrow b\bar{b}$ candidate	12.1
5	p_T of Z boson candidate	11.5
6	$p_T^{ZZ^*}$	11.3
7	MET	10.3
8	Mass of ZZ^* system	7.7
9	Mass of Z boson candidate	6.1

Table 1.6: Di-electron channel. Relative importance of the input variables in the high mass BDT training.

Rank	Variable	Importance, %
1	Mass of $H \rightarrow b\bar{b}$ candidate	13.8
2	$\Delta R_{b\ jets}$	13.1
3	$\Delta R_{leptons}$	12.9
4	p_T of $H \rightarrow b\bar{b}$ candidate	11.7
5	$p_T^{ZZ^*}$	11.3
6	p_T of Z boson candidate	11.1
7	MET	11
8	Mass of ZZ^* system	8.8
9	Mass of Z boson candidate	6.2

Table 1.8: Di-muon channel. Relative importance of the input variables in the high mass BDT training.

Rank	Variable	Importance, %
1	$\Delta R_{b\ jets}$	13
2	MET	12.2
3	Mass of $H \rightarrow b\bar{b}$ candidate	11.9
4	p_T of $H \rightarrow b\bar{b}$ candidate	11.3
5	p_T of Z boson candidate	11.1
6	$p_T^{ZZ^*}$	10.9
7	$\Delta R_{leptons}$	10.5
8	Mass of ZZ^* system	9.7
9	Mass of Z boson candidate	9.5

Table 1.7: Di-muon channel. Relative importance of the input variables in the low mass BDT training.

The correlations among the input variables are shown in the Figs. 1.16, 1.17, ??, ?. For low mass training, signal samples for mass hypotheses from 250 to 450 GeV are combined together and represent the “signal”. Similarly is done for high mass training - it is a mix of signal samples for mass hypotheses from 500 to 1000 GeV. For background samples, the “background” is a mix of samples of two main background processes: DY in association with jets and $t\bar{t}$ production, weighted by the cross section value.

Below we include figures of the BDT input variables. They are the same variables shown few pages before, but produced by the TMVA package, in this style they allow one a bit easier visual judgement of which variables behave more differently between the signal and the background, see Fig. ??.

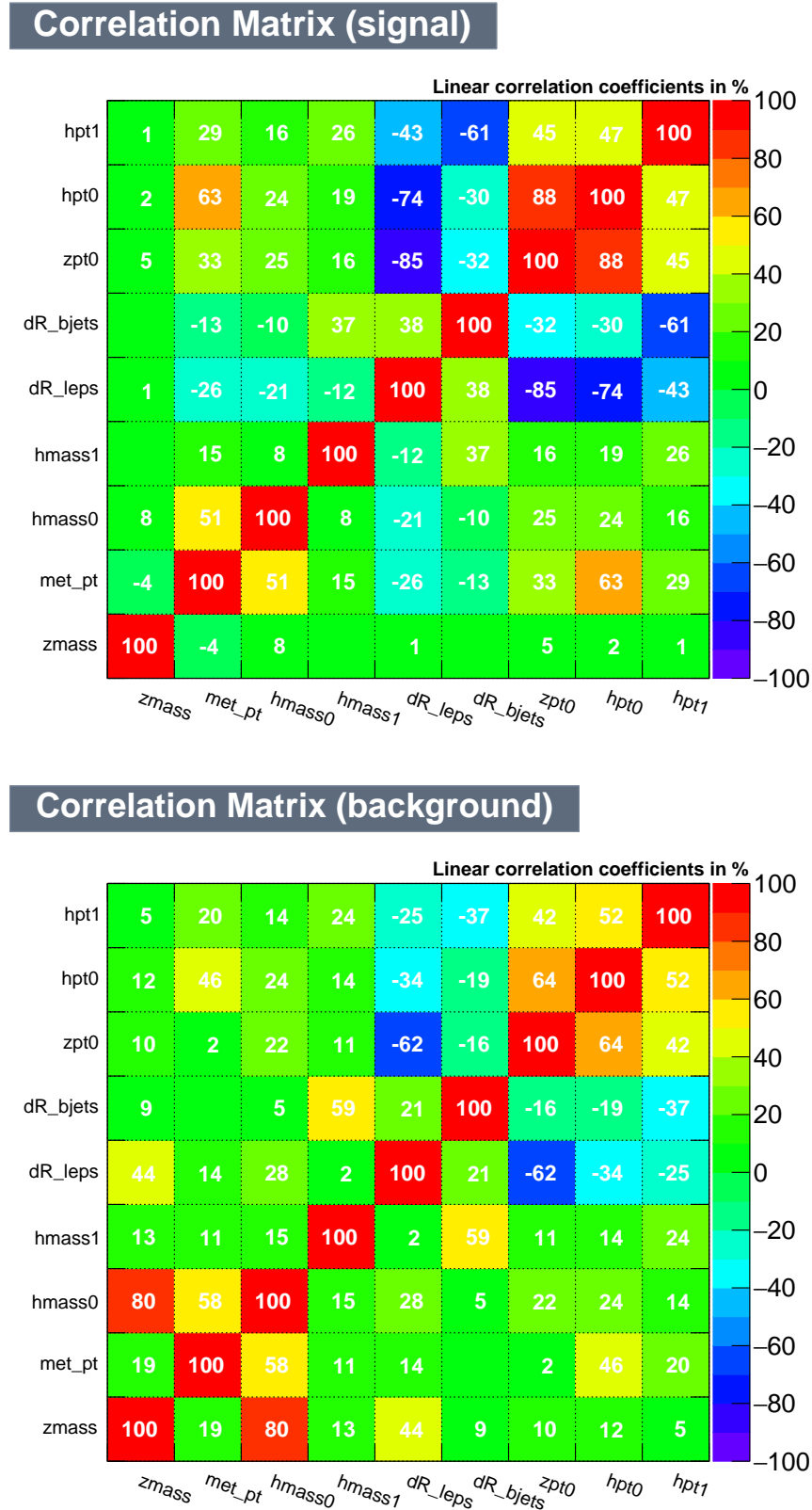
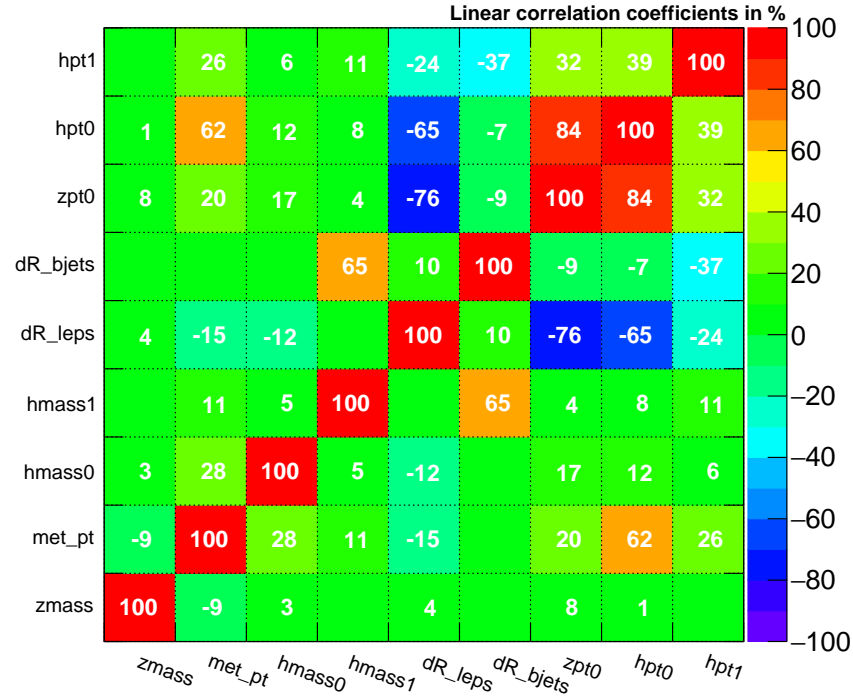


Figure 1.16: Input variable correlations of the di-electron channel, low mass training. Top: signal sample mix. Bottom: background sample mix. The TMVA notation is explained in 1.7.2.

Correlation Matrix (signal)



Correlation Matrix (background)

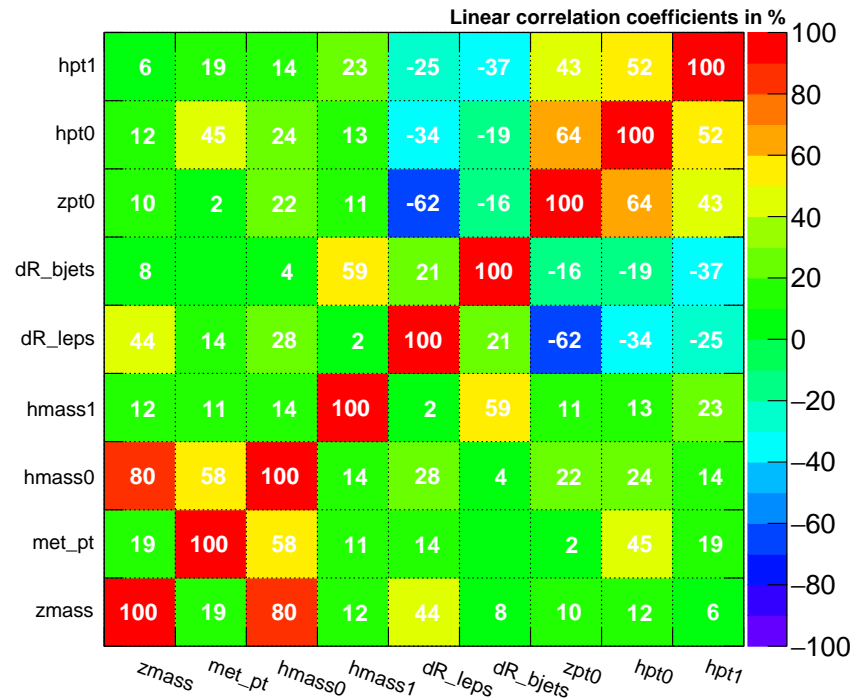


Figure 1.17: Input variable correlations of the di-electron channel, high mass training. Top: signal sample mix. Bottom: background sample mix. The TMVA notation is explained in 1.7.2.

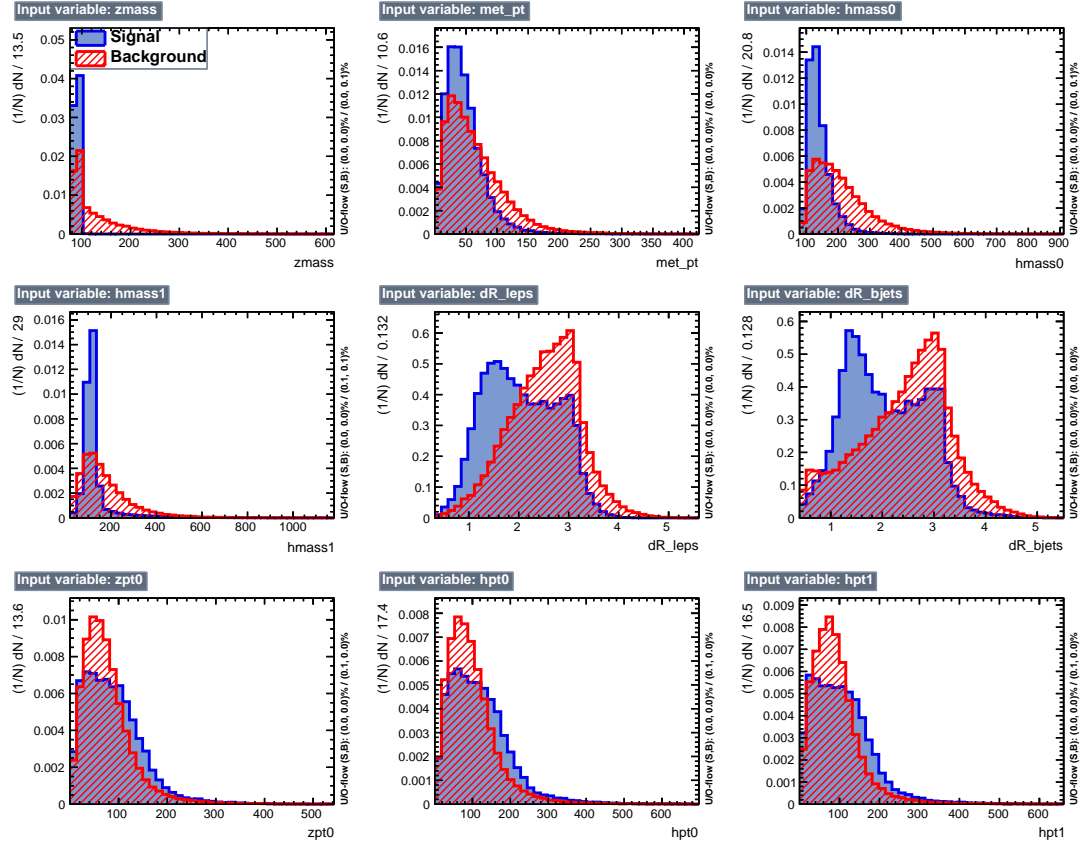


Figure 1.18: Variables used in the low mass training for di-electron channel. Index '1' refers to $H \rightarrow b\bar{b}$ decay and index '0' refers to $H \rightarrow ZZ$ decay. The TMVA notation is explained in 1.7.2.

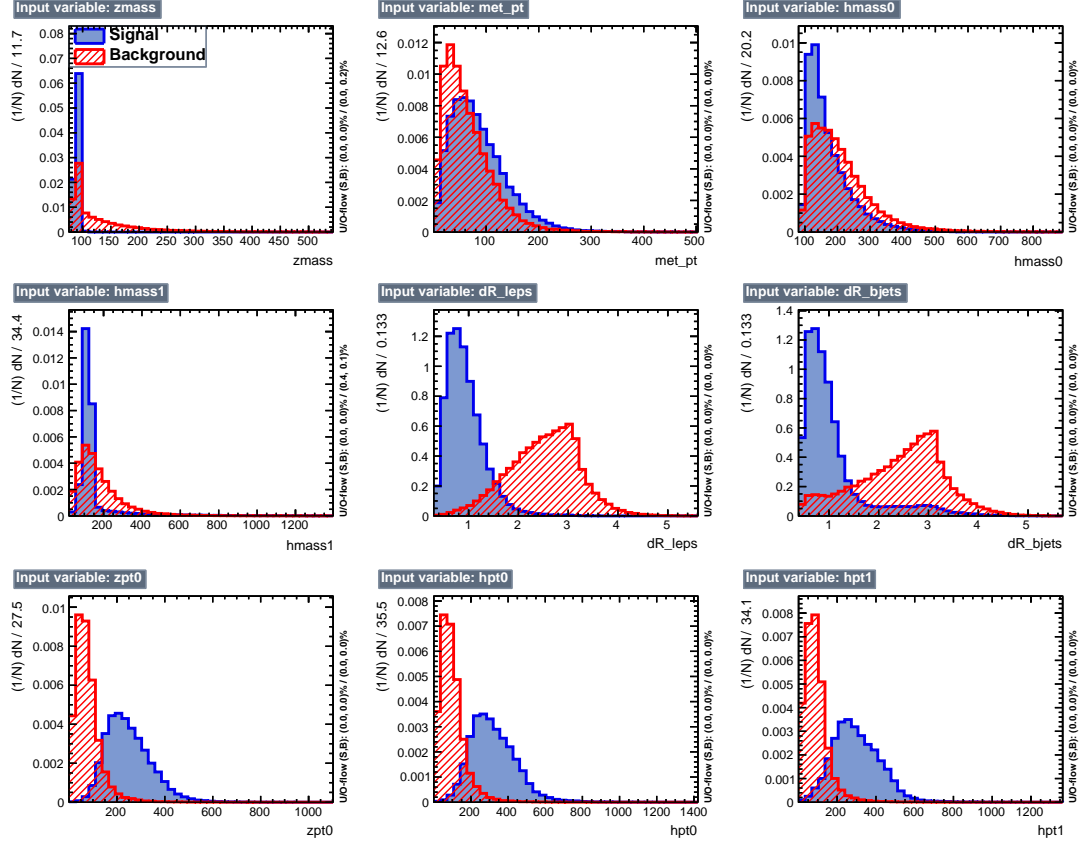


Figure 1.19: Variables used in the high mass training for di-electron channel. Index '1' refers to $H \rightarrow b\bar{b}$ decay and index '0' refers to $H \rightarrow ZZ$ decay. The TMVA notation is explained in 1.7.2.

After the training, the BDT model is created. This model produces the BDT distribution (BDT response), see the Fig. 1.20. This figure shows the BDT output for the di-electron channel, train and test parameters are overlaid. The parameters of the model, such as the number of trees, the allowed number of splits per variable, the

maximum tree depth and others, have been thoroughly studied. It was found that the default TMVA parameters provide this measurement with good performance and, thus, are not changed.

It is difficult to get high performance in the low mass training, since this region corresponds to the range of HH masses where all the background processes are concentrated (Figs. 1.18, 1.19). The rate of background in this region is very high and most variables have similar distributions for signal and background processes. The BDT performance is noticeably better than what can be achieved using a simple linear discriminant method (LD), see Figs. 1.20, 1.21.

Performance of the high mass training can be considered a perfect one, see Fig. 1.19. Most background processes concentrate in the low mass region, therefore, for high mass region even linear discriminant is performing well, see Figs. 1.20, 1.21.

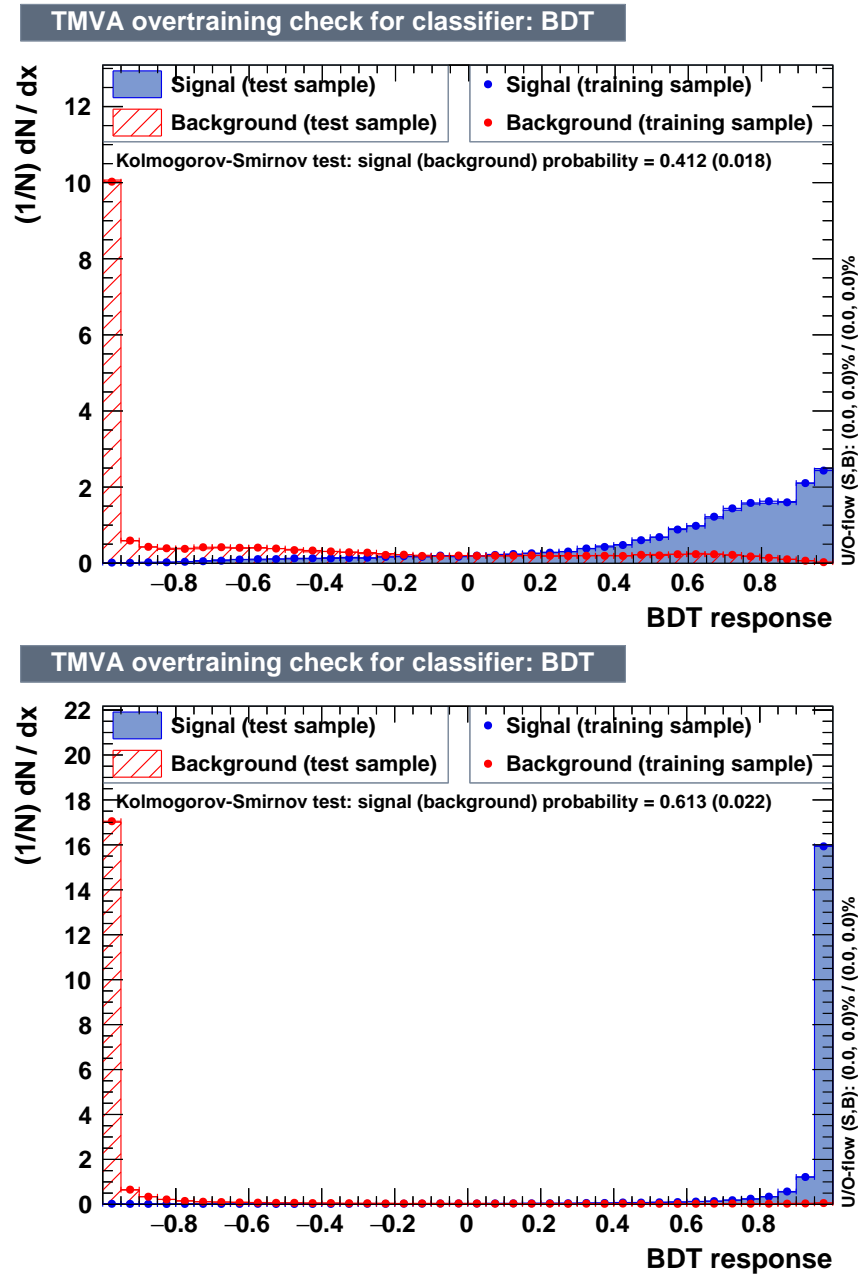


Figure 1.20: BDT discriminants for di-electron channel. Top: low mass training. Bottom: high mass training.

In the machine learning, one needs performance measures to compare several models. Usually for a classification problem, one relies on the Receiver Operating Characteristics curve (ROC) and its Area Under The Curve (AUC). These two are the

most important evaluation metrics for checking the performance for any classification model. The ROC is a curve plotted in the space of signal efficiency and background rejection efficiency, where background rejection is equal to one minus the background efficiency. On the 0 to 1 ranges for axes (values of efficiencies), a diagonal line represents the efficiency of the random guess, which is 0.5. A perfect ROC would bend very close to the top right corner. Such ROC has the AUC almost equal to 1. The ROC curves for di-electron training in low and high mass regions are shown in Fig. 1.21.

ROC can be regarded as a probability curve and, in this case, the AUC represents the degree or measure of signal-background separability. It tells how much model is capable of distinguishing between two given classes. The higher the AUC is, the better the model is at predicting signal as signal-like event and background as background-like event.

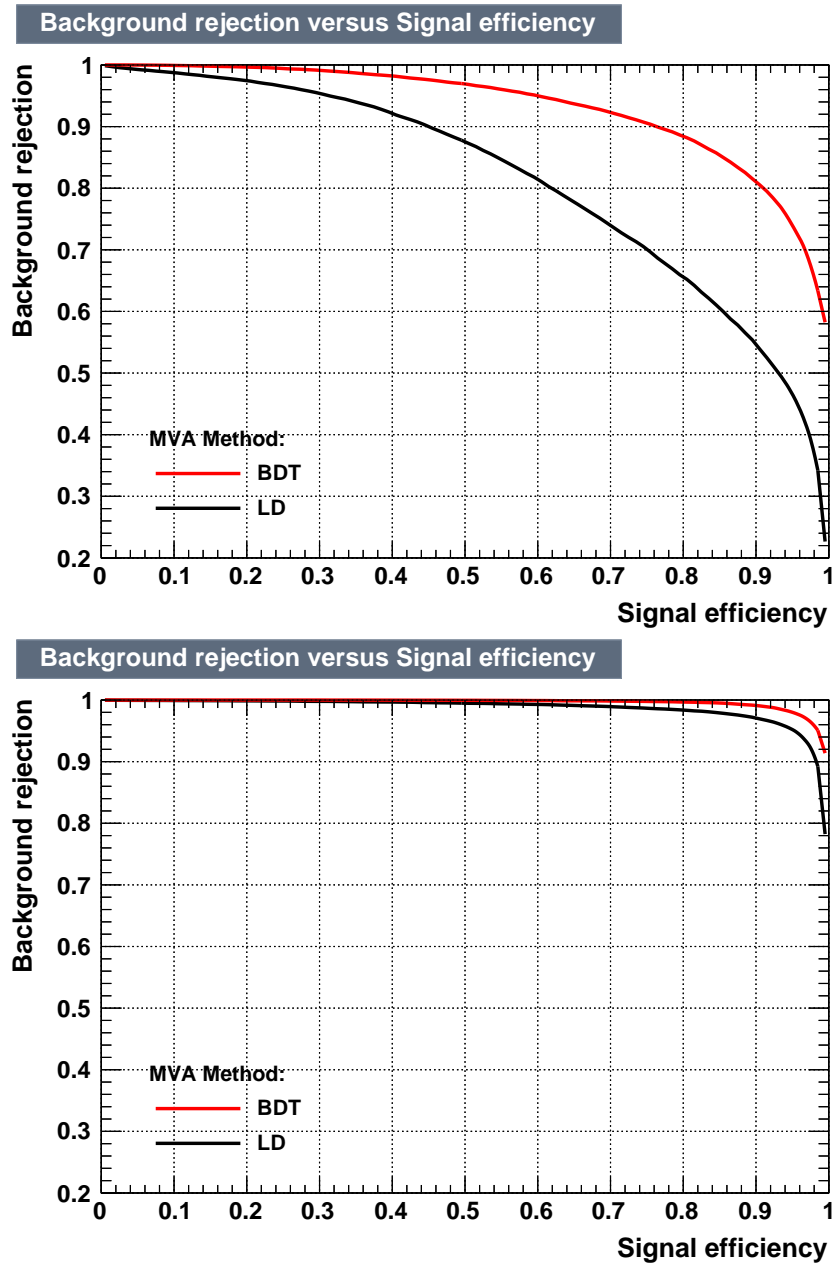


Figure 1.21: ROC curves for di-electron channel. Top: low mass training. Bottom: high mass training.

For two given signal efficiencies, one would prefer the model, which has the lower background efficiency, or in other words, the higher background rejection efficiency. In practice, when AUCs are close to one and ROCs are similar, one compares AUCs

directly and decides which model to use based on the AUC value.

Finally, we provide the figures of the BDT discriminant in the SR. The plots are shown for the 300 GeV radion decaying in the di-electron and di-muon channels. Both figures are of the post-fit type.

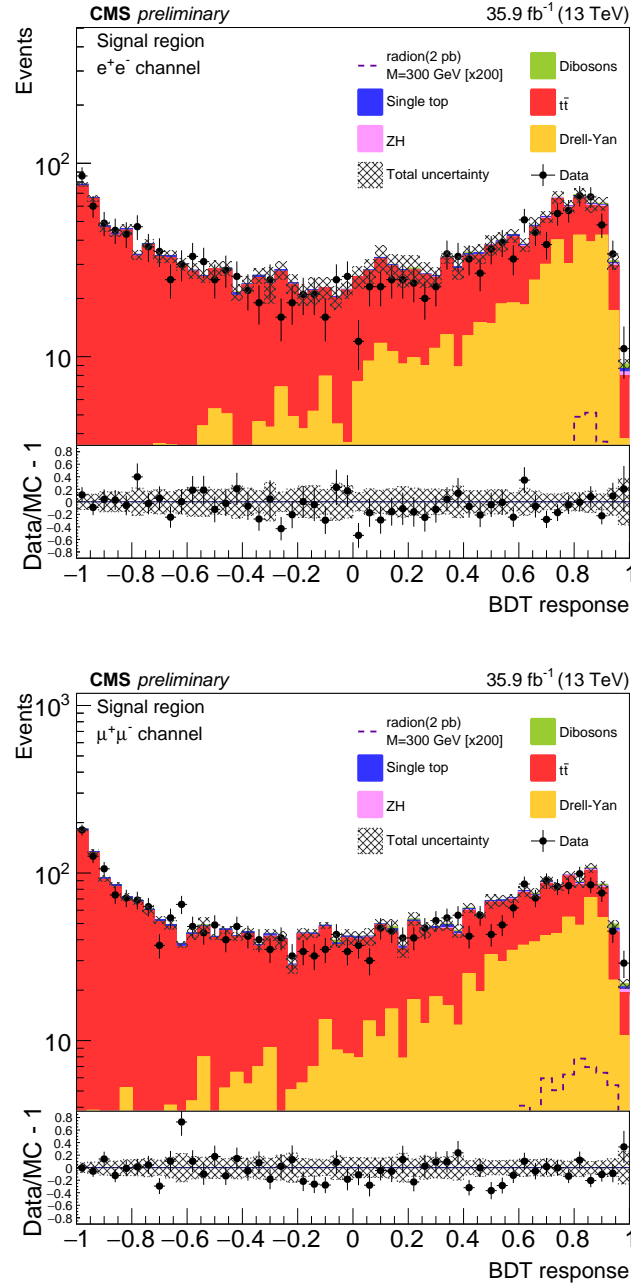


Figure 1.22: BDT distributions for the radion case, electron(muon) channel is shown at the top(bottom). Signal region is presented, 300 GeV mass hypothesis. For electrons the selection is at 0.4, for muons at 0.7, as is described in Section 1.7.3.

Table 1.9: The BDT selection values used in this measurement.

Channel	260 and 270 GeV	300 and 350 GeV	400 and 450 GeV	600 GeV to 1000 GeV
Di-muon	0.1	0.7	0.7	0.99
Di-electron	0.4	0.4	0.925	0.99

1.7.3 BDT selection requirement in the signal region

To remove the background contribution in the SR, we apply a BDT requirement to candidates. The requirement is specific to the mass hypothesis and specific to the lepton channel; however, the requirement does not depend on the resonance nature. A simple grid search method has been adopted to find the best BDT selection for each mass point and channel. During the optimisation procedure, we produced the final limits for each value of the considered BDT requirement. Then we determine the value of the BDT requirement that corresponds to the best expected limit. The optimised final values of the BDT selection that are used in this physics analysis are summarised in the Table 1.9.

Then you explain the method you used to choose the cut value, and provide the table of optimized BDT cut values and the efficiencies (those efficiencies that are presently in the Table 5.2 in the PDF).

[Note that not once in my proposal do I mention the MTHH variable. This is because we really look at it after the full selection including the BDT cut, so it appears premature to look at it earlier. I will propose, in my future comments, to define it and look at its distributions in the Statistical Analysis chapter.]

[There is no need to mention all side studies, all optimizations in detail, or all cross checks in the dissertation, as you would certainly agree. Such as: kinematic plots from BDT sidebands, or CR-only fits.]

Table 1.10: Efficiency of the BDT selection requirement. ee channel (top) and $\mu\mu$ channel (bottom).

sample	Efficiency at 300 GeV, [%]	Efficiency at 900 GeV, [%]
signal (bbZZ)	89.2	94.9
signal (bbWW)	75.0	88.4
$t\bar{t}$	28.8	0.2
Drell-Yan	74.2	1.2
Single top	33.1	1.1
ZH	88.8	10.7
Dibosons	90.0	5.0
sample	Efficiency at 300 GeV, [%]	Efficiency at 900 GeV, [%]
signal (bbZZ)	58.1	91.1
signal (bbWW)	25.9	96.3
$t\bar{t}$	13.6	0.2
Drell-Yan	39.0	0.8
Single top	13.0	0.2
ZH	56.0	8.4
Dibosons	51.4	6.2

1.8 Systematic Uncertainties

Systematic uncertainties that affect the sensitivity of our di-Higgs search come from a variety of sources such as theoretical uncertainties on cross sections or proton structure, experimental uncertainties related to the modelling of the detector response, the amount of collected data, and the discrepancies between the simulated samples and the real data.

Systematic uncertainties can be divided into two broad categories: those affecting only the yields of selected events from different processes (the "normalization" uncertainties) and those that, in addition to the change in rate, may distort the shape of the $\tilde{M}_T(\text{HH})$ distribution used in the extraction of the limits (the "shape" uncertainties).

1.8.1 Normalization uncertainties

The sources of systematic uncertainties that affect normalizations are discussed in the list below. The sizes of some systematic uncertainties may vary depending on the resonance mass hypothesis and the decay channel of the leptonically decaying Zboson, in which cases ranges of the uncertainty values are listed. Normalization uncertainties discussed in this section do not affect the normalizations of the $t\bar{t}$ and DY backgrounds because those are determined from data during the simultaneous fit of the signal and control regions.

- **Luminosity** - CMS estimated this uncertainty on the integrated luminosity of the CMS 2016 data set to be 2.5% [?]. This uncertainty directly affects the expected event yields for the signal processes as well as all background processes except for the two dominant backgrounds, DY and $t\bar{t}$.
- **Pileup** - Signal and background event yields depend on the accuracy of the reproduction of pileup interactions in each simulated event. The effect of pileup is considered on each process. The recommended nominal value of 69.2 mb is used for the total inelastic pp cross section, for Down and Up variations, the values of 66.02 and 72.38 mb are used respectively, reflecting the imperfect knowledge of the total inelastic proton-proton interaction cross section at 13 TeV. The effect is seen only in the normalization and we, thus, consider this a normalization uncertainty and assign the value of 6%.
- **Proton PDF** - The systematic bias associated with the limited knowledge of the interacting proton content is evaluated using an ensemble of a hundred of PDF replicas from the NNPDF set [?] following the PDF4LHC prescription [?,?]

and the RMS of the resulting process normalizations is taken as a measure of the bias. It is found to be of order 5%.

- QCD scales** - Theoretical uncertainties in the QCD factorization and renormalization scales affect the expected yield of the signal and background events, excluding the $t\bar{t}$ and DY yields as mentioned earlier. This uncertainty is estimated by varying independently these two scales in simulation by factors 0.5 and 2 with respect to the nominal values of the scales. The unphysical cases with one of the scales fluctuating up while the other fluctuates down are discarded. In each bin of the HH transverse mass distribution the maximum and minimum variation are used to build an envelope around the nominal shape, resulting in the effect of the size 4-6% on the processes' yields.
- Missing transverse energy/momentum** - Clustered energy in jets and leptons undergo energy corrections during event reconstruction, however, neutral hadrons and photons that do not belong to any jet ("unclustered energy") and jets with low transverse momenta (below 10 GeV) lack such corrections. This results in a small systematic bias in the reconstructed missing transverse momentum. \cancel{E}_T enters the $\tilde{M}_T(\text{HH})$ variable, thus the effect of the unclustered energy has to be studied. We shift the energy of each particle not contained in jets or contained in low- p_T jets by its uncertainty Up and Down. Such variations affect the event yields of signal and background processes at about 3% level but do not have a visible effect on the shape of the HH transverse mass, thus this source is categorised as a "normalization" systematic source.

1.8.2 Shape uncertainties

Several sources of systematic uncertainties affect not only the rate but also the shapes of various kinematic distributions which are inputs to the BDT or a part of the $\tilde{M}_T(\text{HH})$ construction, the BDT discriminant itself, and the shape of the $\tilde{M}_T(\text{HH})$ distribution. Each source is varied separately within one standard deviation up and down, and the effect is propagated through all related variables resulting in the nominal shape of the HH invariant mass distribution and two modified shapes corresponding to the Up and Down variations. Such triplet of shapes is prepared for each channel, each mass hypothesis, and for all processes.

All these shapes are fit simultaneously in the signal extraction likelihood fit. The discussion of these sources of uncertainties follows.

- **Lepton efficiency** - The effect of the detector on the reconstruction of the lepton: identification and isolation selection criteria, and the requirement to pass trigger selection requirements are studied separately and are used to account for data/MC discrepancies. The corrections are derived from large dedicated samples of Zboson decays and also have an error associated with the procedure. The uncertainty on lepton efficiency corrections are derived as a function of lepton p_T and η and is propagated to the final $\tilde{M}_T(\text{HH})$ distributions. The effect of these uncertainties is sub-percent for the muon channel and up to 6% for the electron channel.
- **Jet energy scale** - The uncertainty on the jet energy scale affects $\text{H} \rightarrow b\bar{b}$ mass and p_T , which are inputs to the BDT. In addition, jet energy scale directly affects $\text{H} \rightarrow b\bar{b}$ mass and \cancel{E}_T , which are used during the construction of the HH invariant mass. Jet energy scale is varied Up and Down within one standard deviation of its uncertainty as a function of jet p_T and η , and the effect on the

jet kinematics and on the \cancel{E}_T is calculated and propagated through the steps of the measurement yielding the variation of the HH invariant mass shape. Jet energy scale uncertainty, with all factors combined, has the effect on the yields of the signal and some background components as large as 5 to 10%.

- **Jet energy resolution** - Data and MC a different energy resolution, which also affects the final $\tilde{M}_T(\text{HH})$ shapes via its effect on the dijet invariant mass for $\text{H} \rightarrow b\bar{b}$ and its effect on the \cancel{E}_T . Jet energy resolution is varied in simulation by one standard deviation as a function of jet p_T and η and the effect is propagated through the steps of the measurement. Its effect on the $\tilde{M}_T(\text{HH})$ yield is typically order of 0.5%.
- **b-tagging and mistagging** - The efficiency to tag a q_b -jet and the probability to misidentify a different flavor or a gluon jet and tag it as a q_b -jet is corrected in MC samples by factors derived from flavor-enhanced jet samples. The uncertainties on these corrections are propagated through the whole analysis setup. The effect of the q_b -tagging efficiency (mistagging/flavor misidentification) is about 5% (7–10%) for the Drell-Yan process and at the sub-percent level for other processes (7–10%).
- **Bin-by-bin uncertainties** - Since the available statistics for the simulated MC samples is limited, the lack of events in some bins of the $\tilde{M}_T(\text{HH})$ distribution is addressed by bin-by-bin (BBB) uncertainty. This effect may result in sizeable fluctuations of the bin content of the HH invariant mass shapes that enter the likelihood fit. Therefore, for each bin of the HH invariant mass distributions an individual nuisance parameter is added to the likelihood fit with the Gaussian constraint of one standard deviation of the yield uncertainty in that bin.

1.9 Statistical Analysis

The results in this measurement are obtained with the maximum likelihood fit. We perform a simultaneous fit of the SR and both CRs for both dielectron and dimuon channels using the likelihood function constructed as a product of Poisson terms over all bins of the input $\tilde{M}_T(\text{HH})$ distributions in the three regions (SR, CRDY, CRTT) with Gaussian terms to constrain the nuisance parameters:

$$L(r_{\text{signal}}, r_k | \text{data}) = \prod_{i=1}^{N_{\text{bins}}} \frac{\mu_i^{n_i} \cdot e^{-\mu_i}}{n_i!} \cdot \prod_{j=1}^{N_{\text{nuisances}}} e^{-\frac{1}{2}\theta_j^2}$$

where the product index i refers to the bin of the input distributions, the product index j refers to uncertainties accounted for by the fit model, and n_i is the number of observed data events in the bin i . The mean value for each of the Poisson distributions is computed as:

$$\mu_i = r_{\text{signal}} \cdot S_i + \sum_k r_k \cdot B_{k,i},$$

where k refers to the background process k , and $B_{k,i}$ is the content of the bin i of the background shape for a process k , while S_i is the content of the bin i of the signal shape. The parameter r_k sets the normalization of the background process k while r_{signal} is the signal strength parameter, all r parameters are floating freely in the fit. Two values of the signal strength parameter are of special interest: $r_{\text{signal}} = 0$ describes the background-only hypothesis, while $r_{\text{signal}} = 1$ corresponds to the case when the HH cross section matches the cross section used for the initial signal normalization inspired by BSM models, 2pb in our case. The terms θ_j represent

the set of nuisance parameters that are introduced into the likelihood function as Gaussian constraints.

Figure 1.29(1.30) shows the HH transverse mass distributions for the signal and two control regions for both channels for the graviton (radion) resonance mass hypothesis with normalizations and shapes of all components adjusted according to the best-fit values. The signal sample is normalized to the cross section of 2 pb, a typical value for predictions of WED models (e.g., at 300 GeV), and is further scaled, as indicated on the Figure, to make it clearly visible.

With the given 2016 dataset, the fit results show no evidence for HH production through a narrow resonance, whose width is negligible in comparison to experimental resolution, in the mass range from 250 GeV to 1 TeV. Thus, upper 95 % confidence level limits on the HH production cross section are set using the modified frequentist CL_s approach (asymptotic CL_s) [88–90, 108].

The observed and expected 95% upper CL limits for the full mass range and both resonances are listed in Table 1.11. We produce the standard CMS Brazilian-flag type of plot for the limits, shown in Fig. 1.23. The green and yellow bands correspond to one and two standard deviations around the expected limit respectively. Since 450 GeV is the separation boundary between two mass regions: low mass and high mass, the limit calculation is performed with both of the BDTs at 450 GeV, where the discontinuity is seen in the figure. The Figure also shows the expected production cross section for a RS1 KK graviton/RS1 radion in WED models. This cross section is computed in [2] under the assumption of no mixing with the SM Higgs boson.

1.10 Limits Extraction

DROP

Prior to the derivation of the expected limits, we had to make sure their values are the most sensitive limits that our analysis can set. For that, we have done an optimization study finding the best cut value on the BDT discriminant with the idea to yield the lowest (the most sensitive) limit.

1.10.1 Results from the fit

The extraction of the results is performed by what is called at CMS "Binned shape analysis". We used Higgs Combination Tool ("HiggsCombine") [166], which is a framework with the help of which the Higgs boson had been discovered. HiggsCombine is based on the RooStats package that has been very popular in the HEP community for years.

We do a simultaneous fit ($\tilde{M}_T(\text{HH})$ transverse mass distribution is used) of all three regions: signal region and two control regions, to extract both signal strength parameter as well as normalizations of $t\bar{t}$ and Drell-Yan backgrounds. We use the following command to produce expected limits with the Asimov [89] toy dataset :

```
combine -M Asymptotic -t -1 -v 3 -m massValue --run blind comb_card_massValue.txt.
```

The results in the Table 1.11 are final limits produced with the combined data of electron and muon channels. The corresponding plots, from which these numbers were extracted, are shown on the Figs. 1.23.

Full postfit distributions (the naming emphasises that all regions are used in the fit, signal region included) are shown on the Figs. 1.29 for the graviton case and Figs. 1.30 for the radion case.

This the first ever bbZZ analysis performed at CERN with the real data. We use the standard set of the CMS reconstructed physics objects. Below, we describe reconstruction of each separately: electrons, muons, jets and b jets, and MET.

Table 1.11: The expected and observed HH production cross section upper limits at 95% CL for different narrow resonance graviton (top) and radion (bottom) mass hypotheses for both dielectron and dimuon channels combined.

Mass, GeV	Observed Limit, pb	Expected Limit, pb
250	253.5	589.1
260	272.2	585.9
270	274.4	537.5
300	380.0	434.4
350	330.6	309.4
400	90.4	119.9
450	59.8	63.3
500	31.0	36.6
550	14.5	20.2
600	9.8	12.7
650	18.5	11.1
700	16.1	10.1
750	13.7	8.8
800	10.1	6.5
900	8.1	4.8
1000	5.8	4.2

Mass, GeV	Observed Limit, pb	Expected Limit, pb
250	107.3	297.7
260	170.8	410.9
270	207.0	470.3
300	451.7	496.9
350	532.6	496.9
400	155.7	171.1
450	89.3	82.0
500	36.0	54.4
550	18.7	28.5
600	13.2	19.6
650	24.6	17.2
700	16.4	12.0
750	13.9	10.4
800	12.6	9.8
900	6.9	5.6
1000	5.7	4.5

1.11 $bbZZ$ measurements and combination of all HH channels

I suggest to change the title to ?Discussion?. Or ?Combination of HH measurements in different channels?. I'd suggest the former.

The discussion as it is need to be re-thought. Many of the points are fine to discuss, however they need to be rearranged and the language improved. I will make a suggestion here, but I have not commented extensively the yellow notes in the PDF, the reshuffling is too significant. Still, please see some minor notes in [1] in section 10. On the positive side, it is not too much work, just one page.

Start saying that in searches for a process when intermediate particles can decay through a variety of channels, a common experimental approach is to search for multiple final states in parallel, and, subsequently, combine the results, such as limits on a cross section of a physics process such as production of a heavy resonance, into a single result. At CMS, the Higgs program includes searches for HH production, both of the SM and BSM type, in multiple channels that are published as individual papers. For HH, the individual channels include many of the channels seen in Fig.XX[with Rami's photo]. This is usually followed by the final paper that presents the combined result of all individual channels, the ?grand combination?. This measurement, the search for a resonant production of the HH system decaying through the intermediate $bbZZ$ state into the final state $2b2l2\nu$ is completed, approved by the CMS collaboration [give reference to your PAS], and is shown at conferences. This measurement is, at the time of this writing, is being combined with a similar channel, where the HH system decays through the same intermediate state $bbZZ$ into the final state $2b2l2\text{jets}$, and a paper is will be submitted to the Physical Review D shortly after the defense of this dissertation. Once the 13 TeV dataset is fully analyzed, CMS

plans to release the grand combination paper for the HH production search that is based on the bbZZ channel discussed here as well as many other channels. As of this writing, the best available grand combination from the CMS experiment is based on a partial 13 TeV dataset analysis published in [xx] that includes a subset of all channels. That paper does not include the present measurement, which would be found just above the bbWW graph seen in the legend as $\nu\bar{\nu}\nu\bar{\nu}$. As can be seen from the figure, the most sensitive channels are the bbgg for the mass region below 500 GeV, and the bbbb channel for higher masses. Here, discuss the prospects. Say that while no individual channel measurement is not going to be sensitive enough to see a resonant HH production at the level predicted by WED, the grand combination for the full dataset may be able to see the process if it exists and approach the sensitivity of order of picobarns. With more data taken in Run 3 and the HL-LHC period, the BSM theories discussed here will be probed more and more stringently. However, the ability for a collider experiment to see the SM production of the HH system is at least a decay, or more, in the future. Next, you can explain that a projected sensitivity for a measurement based on the full data set expected to be collected with the HL-LHC is such and such, and will be able to probe the SM production at this level. Finally, you can say that whether searching for a BSM resonant production on the SM production of HH, we need new data + new methods, etc, which is in progress in CMS, etc. You can keep the last paragraph as it is as a jumping board into the conclusions.

Even for the HL-LHC with almost 3 ab^{-1} of data, none of the HH analyses can reach the discovery sensitivity, thus the goal for all HH analyses now and in the nearest future is to contribute to the grand combination and only in this collaborative way to achieve the desired sensitivity. From the recent results of the HL-LHC HH combination projection analysis [178]: "the statistical combination of the five decay channels results in an expected significance for the standard model HH signal of 2.6σ ".

This is a clear sign that more data are needed. However, many Higgs analysts would agree that new statistical and MVA tools should be developed/employed. Thus, the next iteration of this analysis will most likely use a sophisticated neural network not only for the signal-background separation, but also for lepton reconstruction, etc.

This analysis is the search for the double Higgs boson production mediated by the intermediate graviton (and separately) by the radion in the $bbZZ$ channel with the 2 b jets, 2 leptons, 2 neutrinos final state with the $35.9fb^{-1}$ 2016 dataset. According to the CMS Physics Coordination, for the paper in PRD this analysis has to be combined with the other $bbZZ$ analysis, which is focused on the 2 bjets, 2 leptons, 2 jets signature. The mass range to be covered in the combined measurement is also from 250 GeV to 1000 GeV.

Regarding the latest grand combination for the spin 0 and spin 2 cases [179] shown at the Fig. 1.24, the results are obtained for the extended mass range going from 250 GeV up to 3000 GeV, but no significant excess is found. The combination is done for the mass regions where at least two decay channels could contribute. Overall, $b\bar{b}\gamma\gamma$ is the most sensitive channel in the low mass region and $b\bar{b}b\bar{b}$ in the higher mass region (above ~ 500 GeV).

This concludes the discussion of analysis details and in the next chapter we will summarise the main ideas that have been covered throughout this thesis.

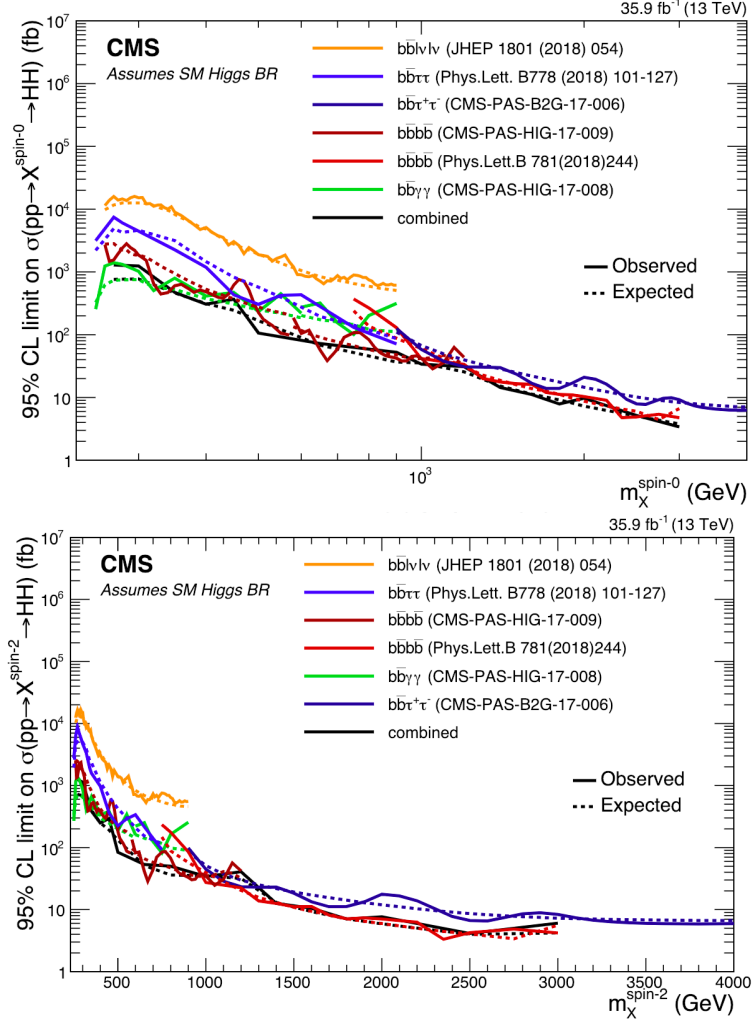


Figure 1.24: Combination of HH channels using 2016 data. Expected (dashed) and observed (solid line) 95% CL exclusion limits are shown. The results describe the production cross section of a narrow width spin 0 (top) and spin 2 (bottom) resonance decaying into a pair of SM Higgs bosons.

1.11.1 Data and MC comparison

FROM SEAN

The first such correction addresses the difference between the $pT(V)$ spectrum in data and the V +jets MC samples. The $pT(V)$ distribution is harder for simulation than for data because the simulation does not include higher-order electroweak

corrections.[103] The $V + \text{jets}$ samples are therefore reweighted as a function of the $p_T(V)$ to apply the NLO electroweak correction shown in Figure 4-5 which accounts for discrepancies of up to 10

A third correction addresses the discrepancy between the di-jet invariant mass $m(jj)$ distribution in data and the LO $V + \text{jets}$ MC samples. Although NLO $V + \text{jets}$ MC samples are readily available and show good agreement with data for the $m(jj)$ distribution, they are not used by the analysis because their limited statistical power results in an over 10% Higgs boson decay $??(jj)$ is derived as a ratio of the NLO to LO $V + \text{jets}$ samples following the procedure outlined in Ref. [28]. An example of this ratio is shown in Figure 4-6. These reweighting functions improve the agreement between data and the LO $V + \text{jets}$ 89 samples for the $m(jj)$ and $p_T(V)$ distributions while demonstrating a negligible effect on the remaining distributions. The full reweighting is assessed as a systematic uncertainty.

BDT selection is applied in the signal region only, we are not cutting on BDT for control regions, therefore, all the mass points belonging to the low mass region (and separately to the high mass region) have the same background and data distributions. Thus, we provide plots for two mass points: one mass point representing low mass region, 300 GeV, and one mass point representing high mass region, 900 GeV. Signal $bbZZ$ and $bbWW$ rates for all plots are multiplied additionally by a factor of 500 purely for the visualization purpose and do not go in the real analysis.

Postfit plots that include SR in the simultaneous fit with control regions, hence a common jargon name "Full postfit" plots, in contrast to the control regions only type of the fit, or a control regions plus signal region sideband. Figures 1.29 - 1.30 show data and MC comparison in the SR, CRDY, and CRTT. For both ee and $\mu\mu$ channels, low and high mass regions. The latest style plots produced for the analysis public document (Physics Analysis Summary called "PAS") can be found at Fig. 1.29

for the graviton case and Fig. 1.30 for the radion case.

Distributions of nine variables that go into the BDT have been studied in depth during the pre-approval process and are available in the Appendix of the analysis note [159]. All variables show good data/MC agreement after applying postfit scale factors (not to be confused with the POG recommended scale factors in the section below). The most important variables in this analysis, namely the BDT itself and the variable that we fit, $\tilde{M}_T(\text{HH})$, are shown in the Fig. 1.29 for graviton and in Fig. 1.30 for the radion.

1.11.2 Scale Factors

Electron ID and ISO scale factors, as well as HLT scale factors (Fig. 1.1), have been computed by VHbb group, which ntuples and analysis setup we reutilise. Scale factors have been presented at the EGamma physics object groups (POG) meeting [160] and fully approved. We reuse those scale factors and apply them to our MC samples.

Muon ID scale factors, as well as ISO scale factors, have been derived separately for runs G/H and B/C/D/E/F runs (2016 data at LHC has been split into several "runs") and then luminosity averaged to obtain the final numbers [114]. Tracker scale factors (1.1) are taken from the Muon POG twiki page [115] and used as is. HLT dimuon scale factors were derived by VHbb group and further approved by the muon POG. These scale factors were derived separately for run H (Fig. 1.3) and B/C/D/E/F/G (Fig. 1.2) runs and then luminosity averaged [116]. On top, separate scale factors are calculated for the dZ requirement of `HLT_Mu17_TrkIsoVVL_Mu8_TrkIsoVVL_DZ_v*` OR `HLT_Mu17_TrkIsoVVL_TkMu8_TrkIsoVVL_DZ_v*` triggers, using dilepton events that have already passed the `HLT_Mu17_TrkIsoVVL_Mu8_TrkIsoVVL_v*` OR `HLT_Mu17_TrkIsoVVL_TkMu8_TrkIsoVVL_v*` triggers (Fig. 1.4).

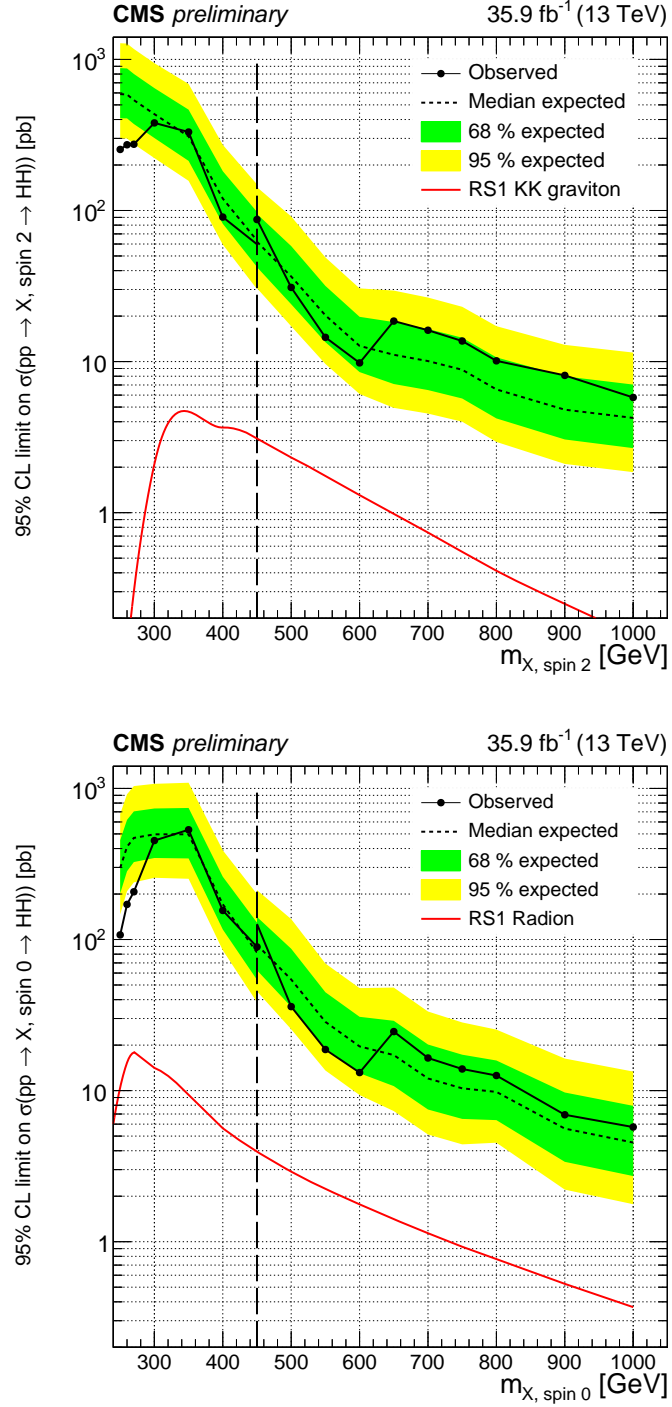


Figure 1.23: Expected (dashed line) and observed (solid line) limits on the cross section of a resonant HH production as a function of the mass of the narrow resonance for both leptonic channels combined. Graviton case is shown at the top and radion case at the bottom. The red line shows a theoretical prediction for the production of a WED particle with certain model assumptions [2].

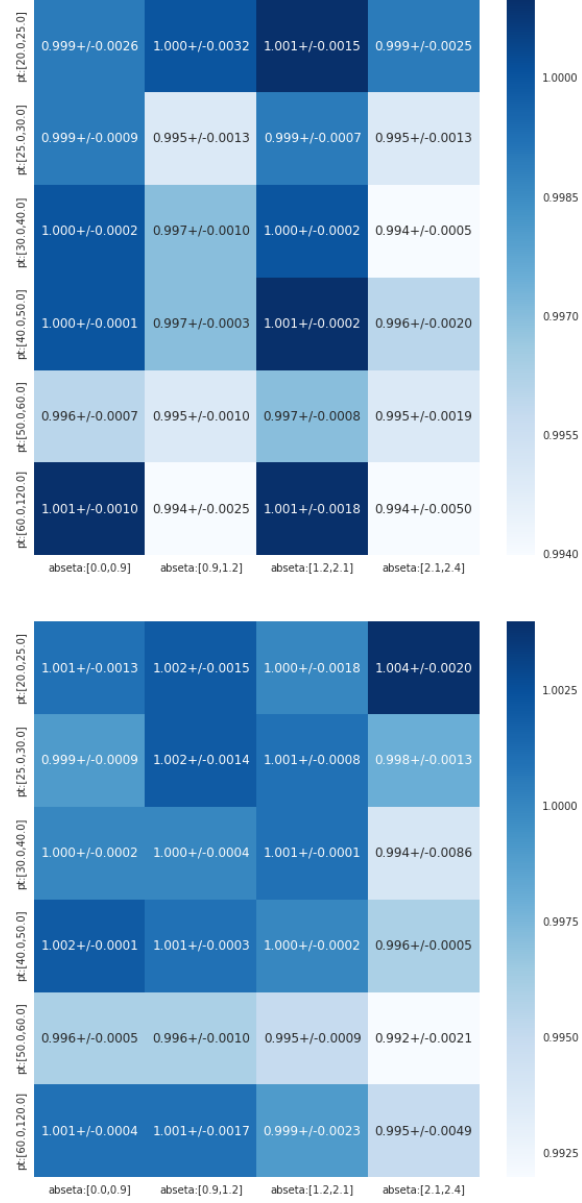


Figure 1.25: Muon ID scale factors in p_T and η bins. Left: runs B to F. Right: runs G and H.

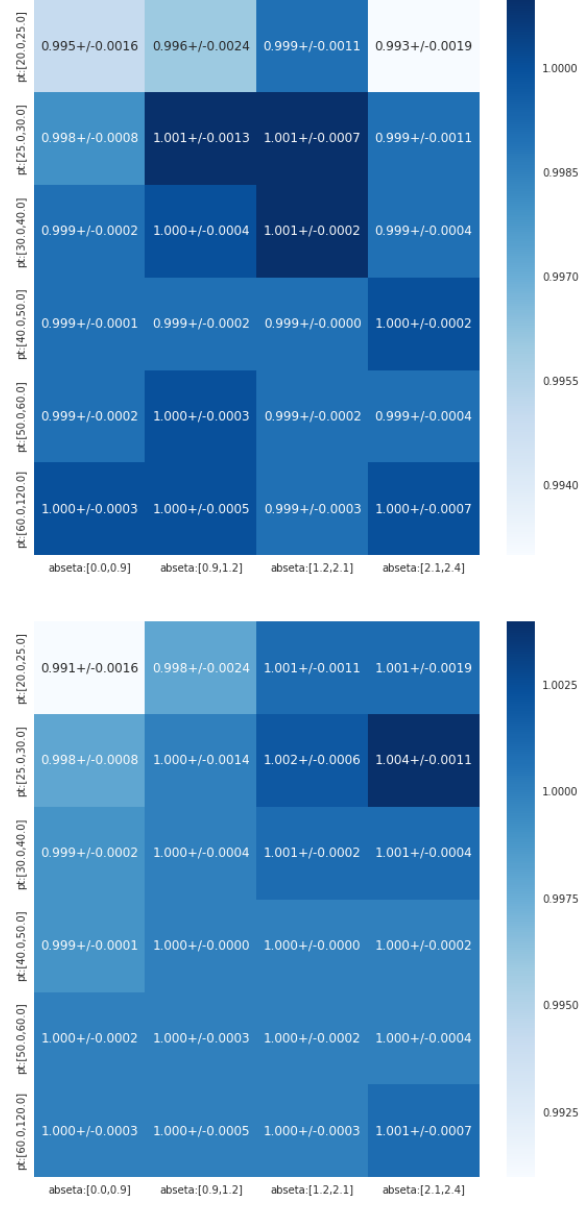


Figure 1.26: Muon ISO scale factors in p_T and η bins. Left: runs B to F. Right: runs G and H.

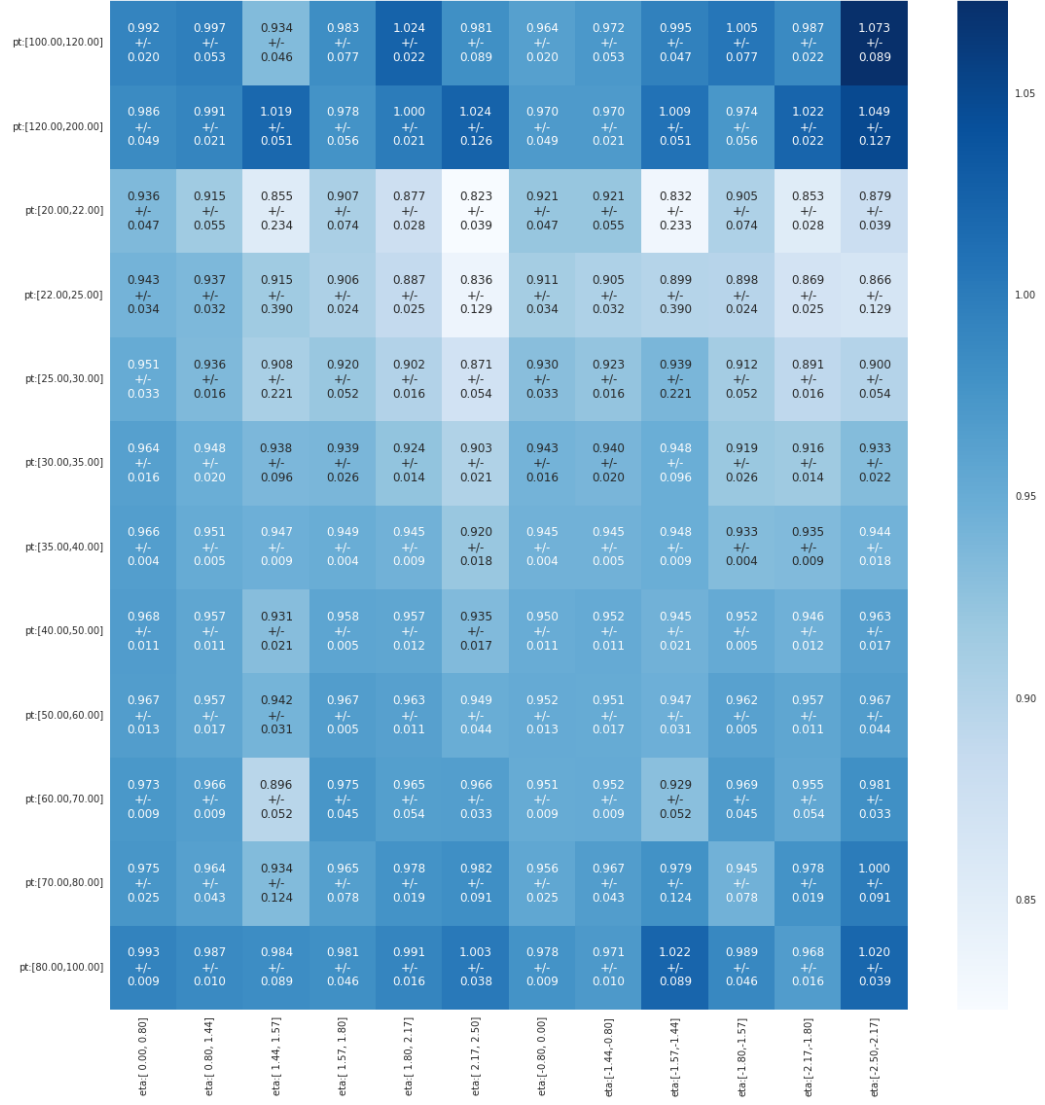


Figure 1.27: Electron ID+ISO scale factors in p_T and η bins.

	2 very loose muons	2 loose muons	mva ID	leading pt and eta gap	iso<0.15	trigger	>=2b-jets, Hbb and Zll cuts
bbWW300		100.0	41.8	21.6	20.3	17.8	16.6
bbZZ300		100.0	87.4	61.6	56.7	43.0	40.7
bbWW900		100.0	53.5	15.8	14.6	10.5	9.9
bbZZ900		100.0	84.0	63.3	59.7	53.6	50.2
	2 very loose electrons	2 loose electrons	mva ID	leading pt and eta gap	iso<0.06	trigger	>=2b-jets, Hbb and Zll cuts
bbWW300		100.0	38.8	18.9	17.4	13.0	10.0
bbZZ300		100.0	68.2	46.3	43.9	24.7	23.1
bbWW900		100.0	38.5	14.9	13.1	5.5	4.8
bbZZ900		100.0	71.4	46.0	43.7	36.0	33.9

Figure 1.28: Cut flow for mm (top) and ee (bottom) channels.

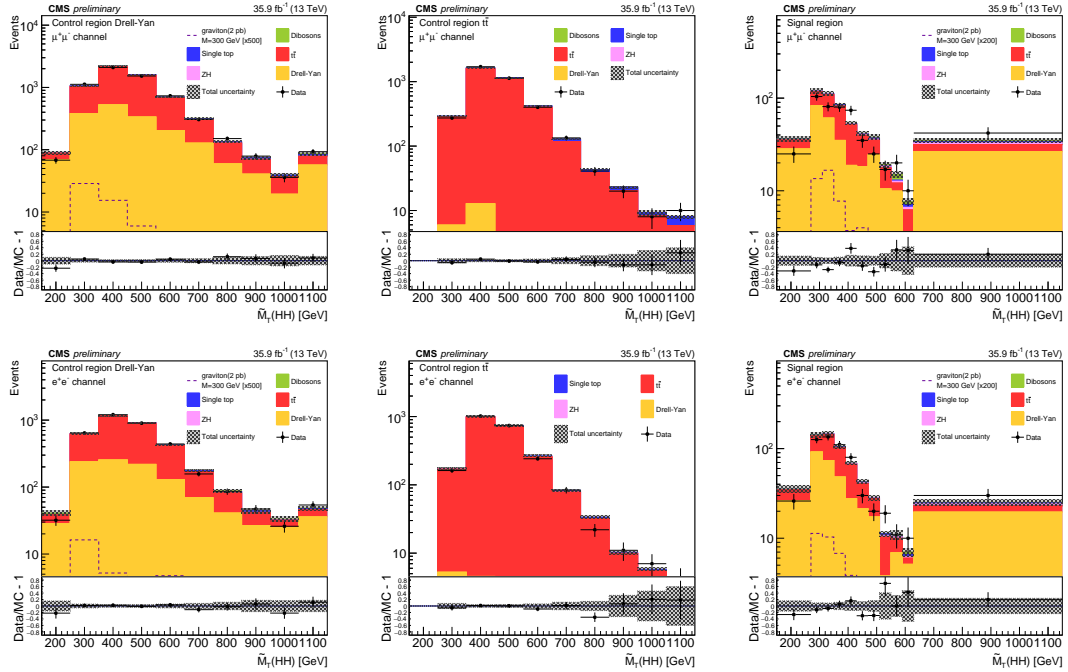


Figure 1.29: Transverse mass of the reconstructed HH candidates for data, the simulated signal graviton sample for the 300 GeV mass hypothesis, and simulated backgrounds scaled according to the fit results. The top row shows the figures for the muon channel while the bottom row is for the electron channel. For each row, the left plot is for the Drell-Yan control region, the middle is for the $t\bar{t}$ control region, and the right is for the signal region. Signal normalization choice is discussed in the text. The crosshatched area represents the sum of statistical and systematic uncertainties.

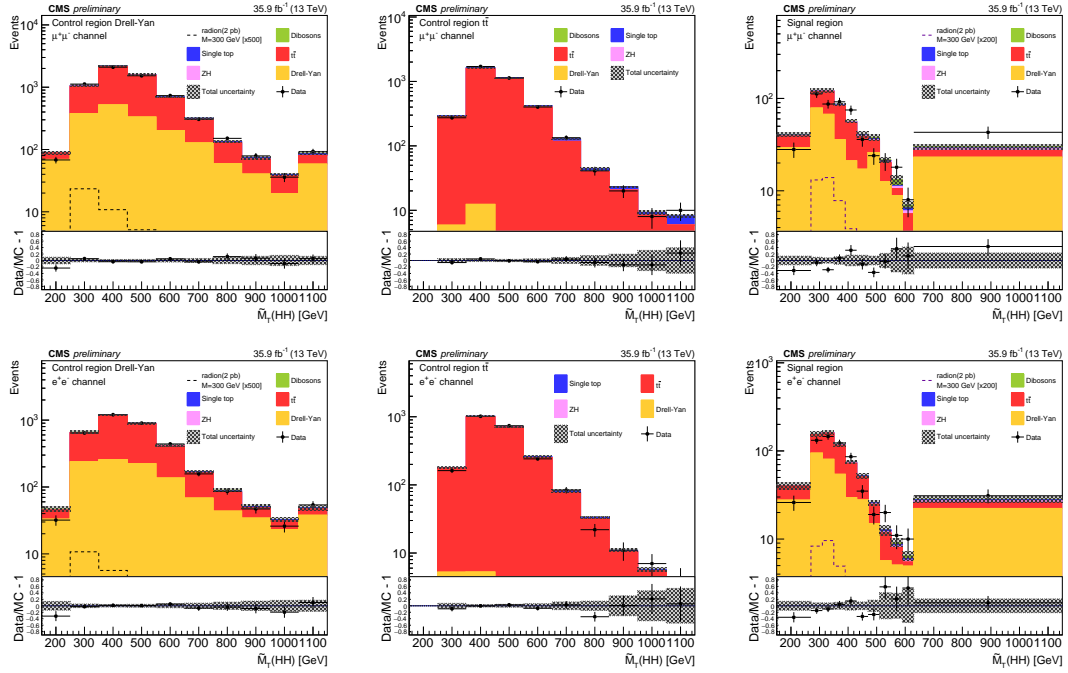


Figure 1.30: Transverse mass of the reconstructed HH candidates for data, the simulated signal radion sample for the 300 GeV mass hypothesis, and simulated backgrounds scaled according to the fit results. The top row shows the figures for the muon channel while the bottom row is for the electron channel. For each row, the left plot is for the Drell-Yan control region, the middle is for the $t\bar{t}$ control region, and the right is for the signal region. Signal normalization choice is discussed in the text. The crosshatched area represents the sum of statistical and systematic uncertainties.

CHAPTER 2

Conclusions

This thesis described the search for the double Higgs boson production mediated separately by the KK graviton and by the radion heavy resonances in the $bbZZ$ channel: one of the Higgs bosons decays to two q_b quarks while the other decays to a pair of Zbosons which, in turn, decay to a pair of neutrinos and a pair of electrons or muons. For this measurement we used 2016 data set with the integrated luminosity of $35.9fb^{-1}$ collected by the CMS experiment at the LHC in the proton-proton collisions at $\sqrt{s} = 13$ TeV.

No statistically significant deviations from the SM predictions for background processes have been observed, and 95% upper confidence limits are reported for production cross section of a KK graviton/radion times the branching fraction of the subsequent decay into an HH system and further to our final state. The limits are derived for resonance masses in the 250 GeV to 1 TeV range.

This analysis became public in November 2018 [181]. Now, according to the CMS Physics Coordination, CMS would like to have a combination of this analysis with the other $bbZZ$ analysis, which is focused on the 2 b jets, 2 leptons, 2 jets signature. Currents plans are to produce a paper for the Physical Review D (PRD), where we will report the best limits for all available $bbZZ$ searches. Of course, prior to the grand $bbZZ$ merge, each analysis combines the data from both dimuon and

dielectron channels. The mass range to be covered in the combined measurement is also from 250 GeV to 1000 GeV.

References

- [1] Michele de Gruttola, Caterina Vernieri, Pierluigi Bortignon, David Curry, Ivan Furic, Jacobo Konigsberg, Sean-Jiun Wang, Paolo Azzurri, Tommaso Boccali, Andrea Rizzi, Silvio Donato, Stephane Brunet Cooperstein , James Olsen, Christopher Palmer, Lorenzo Bianchini, Christoph Grab, Gael Ludovic Perrin, and Luca Perrozzi. Search for the Standard Model Higgs Boson Produced in Association with W and Z and Decaying to Bottom Quarks. http://cms.cern.ch/iCMS/jsp/db_notes/noteInfo.jsp?cmsnoteid=CMS%20AN-2015/168.
- [2] Alexandra Oliveira. Gravity particles from Warped Extra Dimensions, predictions for LHC. 2014.
- [3] CMS Luminosity Measurements for the 2016 Data Taking Period. Technical Report CMS-PAS-LUM-17-001, CERN, Geneva, 2017.
- [4] Erwin Schrödinger. *Statistical thermodynamics; 2nd ed.* Cambridge Univ. Press, Cambridge, 1952.
- [5] Richard Phillips Feynman, Robert Benjamin Leighton, and Matthew Sands. *The Feynman lectures on physics; New millennium ed.* Basic Books, New York, NY, 2010. Originally published 1963-1965.

- [6] David J Griffiths. *Introduction to elementary particles; 2nd rev. version*. Physics textbook. Wiley, New York, NY, 2008.
- [7] E A Davis and Isabel Falconer. *J.J. Thompson and the discovery of the electron*. Taylor and Francis, Hoboken, NJ, 2002.
- [8] Oreste Piccioni. *The Discovery of the Muon*, pages 143–162. Springer US, Boston, MA, 1996.
- [9] Carl Bender. Mathematical physics.
- [10] G. Danby, J-M. Gaillard, K. Goulianos, L. M. Lederman, N. Mistry, M. Schwartz, and J. Steinberger. Observation of high-energy neutrino reactions and the existence of two kinds of neutrinos. *Phys. Rev. Lett.*, 9:36–44, Jul 1962.
- [11] M. L. Perl, G. S. Abrams, A. M. Boyarski, et al. Evidence for anomalous lepton production in $e^+ - e^-$ annihilation. *Phys. Rev. Lett.*, 35:1489–1492, Dec 1975.
- [12] K. Kodama et al. Observation of tau neutrino interactions. *Phys. Lett.*, B504:218–224, 2001.
- [13] Eric W. Weisstein. Fundamental forces.
- [14] S Chandrasekhar. *Newton’s principia for the common reader*. Oxford Univ., Oxford, 2003. The book can be consulted by contacting: PH-AID: Wallet, Lionel.
- [15] Charles W. Misner, Kip S. Thorne, and John Archibald Wheeler. *Gravitation / Charles W. Misner, Kip S. Thorne, John Archibald Wheeler*. W. H. Freeman San Francisco, 1973.

- [16] Hanoeh Gutfreund and Jurgen Renn. *The road to relativity: the history and meaning of Einstein's "The foundation of general relativity" : featuring the original manuscript of Einstein's masterpiece*. Princeton University Press, Princeton, NJ, Apr 2015.
- [17] J. Butterworth. *Smashing Physics*. Headline Publishing Group, 2014.
- [18] A Zee. *Quantum Field Theory in a Nutshell*. Nutshell handbook. Princeton Univ. Press, Princeton, NJ, 2003.
- [19] W N Cottingham and D A Greenwood. *An Introduction to the Standard Model of Particle Physics; 2nd ed*. Cambridge Univ. Press, Cambridge, 2007.
- [20] R. P. Feynman. The theory of positrons. *Phys. Rev.*, 76:749–759, Sep 1949.
- [21] Francis Halzen and Alan Douglas Martin. *Quarks and leptons: an introductory course in modern particle physics*. Wiley, New York, NY, 1984.
- [22] C. Patrignani et al. Review of Particle Physics. *Chin. Phys.*, C40(10):100001, 2016.
- [23] Andrew Wayne. QED and the Men Who Made It: Dyson, Feynman, Schwinger, and Tomonaga by Silvan S. Schweber. *The British Journal for the Philosophy of Science*, 46(4):624–627, 1995.
- [24] Michelangelo L Mangano. Introduction to QCD. (CERN-OPEN-2000-255), 1999.
- [25] Matt Strassler. Of particular significance: Conversations about science with theoretical physicist matt strassler.

- [26] S. L. Glashow. Partial Symmetries of Weak Interactions. *Nucl. Phys.*, 22:579–588, 1961.
- [27] F. Englert and R. Brout. Broken symmetry and the mass of gauge vector mesons. *Phys. Rev. Lett.*, 13:321–323, Aug 1964.
- [28] Peter W. Higgs. Broken symmetries and the masses of gauge bosons. *Phys. Rev. Lett.*, 13:508–509, Oct 1964.
- [29] G. S. Guralnik, C. R. Hagen, and T. W. B. Kibble. Global conservation laws and massless particles. *Phys. Rev. Lett.*, 13:585–587, Nov 1964.
- [30] Pauline Gagnon. *Who cares about particle physics? : making sense of the Higgs boson, the Large Hadron Collider and CERN*. Oxford University Press, 2016.
- [31] Precise determination of the mass of the Higgs boson and studies of the compatibility of its couplings with the standard model. Technical Report CMS-PAS-HIG-14-009, CERN, Geneva, 2014.
- [32] Jennifer Ouellette. Einstein’s quest for a unified theory. *APS*, 2015.
- [33] S. M. Bilenky. Neutrino in Standard Model and beyond. *Phys. Part. Nucl.*, 46(4):475–496, 2015.
- [34] Matthias U. Mozer. Electroweak Physics at the LHC. *Springer Tracts Mod. Phys.*, 267:1–115, 2016.
- [35] Gennadi Sardanashvily. *Noether’s theorems: applications in mechanics and field theory*. Atlantis studies in variational geometry. Springer, Paris, 2016.
- [36] Steven Weinberg. The Making of the Standard Model. *Eur. Phys. J. C*, 34(hep-ph/0401010):5–13. 21 p. ; streaming video, 2003.

- [37] Roger Wolf. *The Higgs Boson Discovery at the Large Hadron Collider*, volume 264. Springer, 2015.
- [38] Jose Andres Monroy Montanez, Kenneth Bloom, and Aaron Dominguez. Search for production of a Higgs boson and a single Top quark in multilepton final states in pp collisions at $\sqrt{s} = 13$ TeV, Jul 2018. Presented 23 Jul 2018.
- [39] Peisi Huang, Aniket Joglekar, Min Li, and Carlos E. M. Wagner. Corrections to di-Higgs boson production with light stops and modified Higgs couplings. *Phys. Rev.*, D97(7):075001, 2018.
- [40] Matthew J. Dolan, Christoph Englert, and Michael Spannowsky. New Physics in LHC Higgs boson pair production. *Phys. Rev.*, D87(5):055002, 2013.
- [41] Shinya Kanemura, Kunio Kaneta, Naoki Machida, Shinya Odori, and Tetsuo Shindou. Single and double production of the Higgs boson at hadron and lepton colliders in minimal composite Higgs models. *Phys. Rev.*, D94(1):015028, 2016.
- [42] Albert M Sirunyan et al. Search for Higgs boson pair production in the $\gamma\gamma b\bar{b}$ final state in pp collisions at $\sqrt{s} = 13$ TeV. 2018.
- [43] Lisa Randall and Raman Sundrum. A Large mass hierarchy from a small extra dimension. *Phys. Rev. Lett.*, 83:3370–3373, 1999.
- [44] Alexandra Oliveira. Gravity particles from Warped Extra Dimensions, predictions for LHC. 2014.
- [45] Kunihiro Uzawa, Yoshiyuki Morisawa, and Shinji Mukohyama. Excitation of Kaluza-Klein gravitational mode. *Phys. Rev.*, D62:064011, 2000.
- [46] Walter D. Goldberger and Mark B. Wise. Modulus stabilization with bulk fields. *Phys. Rev. Lett.*, 83:4922–4925, 1999.

- [47] H. Davoudiasl, J. L. Hewett, and T. G. Rizzo. Phenomenology of the Randall-Sundrum Gauge Hierarchy Model. *Phys. Rev. Lett.*, 84:2080, 2000.
- [48] Piotr Traczyk and Grzegorz Wrochna. Search for Randall-Sundrum graviton excitations in the CMS experiment. 2002.
- [49] Walter D. Goldberger and Mark B. Wise. Bulk fields in the Randall-Sundrum compactification scenario. *Phys. Rev.*, D60:107505, 1999.
- [50] Sreerup Raychaudhuri and K Sridhar. *Particle physics of brane worlds and extra dimensions*. Cambridge monographs on mathematical physics. Cambridge University Press, Cambridge, 2016.
- [51] Michael Forger and Hartmann Romer. Currents and the energy momentum tensor in classical field theory: A Fresh look at an old problem. *Annals Phys.*, 309:306–389, 2004.
- [52] Lisa Randall and Raman Sundrum. Large mass hierarchy from a small extra dimension. *Phys. Rev. Lett.*, 83:3370–3373, Oct 1999.
- [53] Roberto Contino, Margherita Ghezzi, Mauro Moretti, Giuliano Panico, Fulvio Piccinini, and Andrea Wulzer. Anomalous Couplings in Double Higgs Production. *JHEP*, 08:154, 2012.
- [54] Chuan-Ren Chen and Ian Low. Double take on new physics in double Higgs boson production. *Phys. Rev.*, D90(1):013018, 2014.
- [55] Giuliano Panico. Prospects for double Higgs production. *Frascati Phys. Ser.*, 61:102, 2016.
- [56] Sebastien Wertz and Vincent Lemaître. Search for Higgs boson pair production in the $b\bar{b}\ell\nu\ell\nu$ final state with the CMS detector, 2018.

- [57] Luca Cadamuro, Yves Sirois, and Roberto Salerno. Search for Higgs boson pair production in the $b\bar{b}\tau^+\tau^-$ decay channel with the CMS detector at the LHC. Recherche de la production de paires de bosons de Higgs dans le canal de désintégration $b\bar{b}\tau^+\tau^-$ avec le détecteur CMS auprès du LHC, Sep 2017. Presented 05 Oct 2017.
- [58] Thomas Schörner-Sadenius. *The Large Hadron Collider: harvest of run 1*. Springer, Cham, 2015.
- [59] CERN. *Large Hadron Collider in the LEP Tunnel*, Geneva, 1984. CERN.
- [60] Cecile Noels. Literature in focus - The Large Hadron Collider: A Marvel of Technology. Literature in focus - The Large Hadron Collider: A Marvel of Technology. (BUL-NA-2009-414. 51/2009):11, Dec 2009.
- [61] John Hauptman. *Particle physics experiments at high energy colliders*. 2011.
- [62] CMS Collaboration. The Phase-2 Upgrade of the CMS Tracker. Technical Report CERN-LHCC-2017-009. CMS-TDR-014, CERN, Geneva, Jun 2017.
- [63] Philippe Bloch, Robert Brown, Paul Lecoq, and Hans Rykaczewski. *Changes to CMS ECAL electronics: addendum to the Technical Design Report*. Technical Design Report CMS. CERN, Geneva, 2002.
- [64] *The CMS hadron calorimeter project: Technical Design Report*. Technical Design Report CMS. CERN, Geneva, 1997.
- [65] G Baatian, Albert M Sirunyan, Virgil E Emeliantchik, Igor Barnes, Alvin T Laasanen, and Arnold Pompos. Design, Performance, and Calibration of CMS Hadron-Barrel Calorimeter Wedges. Technical Report CMS-NOTE-2006-138. 1, CERN, Geneva, May 2007.

- [66] CMS Collaboration. The Phase-2 Upgrade of the CMS Muon Detectors. Technical Report CERN-LHCC-2017-012. CMS-TDR-016, CERN, Geneva, Sep 2017. This is the final version, approved by the LHCC.
- [67] Vardan Khachatryan et al. The CMS trigger system. *JINST*, 12(01):P01020, 2017.
- [68] G. Bauer et al. The CMS data acquisition system software. *J. Phys. Conf. Ser.*, 219:022011, 2010.
- [69] G L Bayatian, S Chatrchyan, H Hmayakyan, A Poblaguev, M E Zeller, and B S Yuldashev. *CMS Physics: Technical Design Report Volume 1: Detector Performance and Software*. Technical Design Report CMS. CERN, Geneva, 2006. There is an error on cover due to a technical problem for some items.
- [70] A. M. Sirunyan et al. Particle-flow reconstruction and global event description with the CMS detector. *JINST*, 12(10):P10003, 2017.
- [71] Serguei Chatrchyan et al. Description and performance of track and primary-vertex reconstruction with the CMS tracker. *JINST*, 9(10):P10009, 2014.
- [72] Albert M Sirunyan et al. Particle-flow reconstruction and global event description with the CMS detector. *JINST*, 12(10):P10003, 2017.
- [73] Giuseppe Cerati et al. Parallelized and Vectorized Tracking Using Kalman Filters with CMS Detector Geometry and Events. 2018.
- [74] Wolfgang Adam, R Frühwirth, Are Strandlie, and T Todor. Reconstruction of Electrons with the Gaussian-Sum Filter in the CMS Tracker at the LHC. Technical Report CMS-NOTE-2005-001, CERN, Geneva, Jan 2005.

- [75] E Chabanat and N Estre. Deterministic Annealing for Vertex Finding at CMS. 2005.
- [76] R Frühwirth, Wolfgang Waltenberger, and Pascal Vanlaer. Adaptive Vertex Fitting. Technical Report CMS-NOTE-2007-008, CERN, Geneva, Mar 2007.
- [77] A. M. Sirunyan et al. Particle-flow reconstruction and global event description with the CMS detector. *JINST*, 12(10):P10003, 2017.
- [78] Andreas Hoecker, Peter Speckmayer, Joerg Stelzer, Jan Therhaag, Eckhard von Toerne, and Helge Voss. TMVA: Toolkit for Multivariate Data Analysis. *PoS, ACAT:040*, 2007.
- [79] Matteo Cacciari, Gavin P. Salam, and Gregory Soyez. The anti- k_t jet clustering algorithm. *JHEP*, 04:063, 2008.
- [80] Identification of b quark jets at the CMS Experiment in the LHC Run 2. Technical Report CMS-PAS-BTV-15-001, CERN, Geneva, 2016.
- [81] A. M. Sirunyan et al. Identification of heavy-flavour jets with the CMS detector in pp collisions at 13 TeV. *JINST*, 13(05):P05011, 2018.
- [82] Lior Rokach. Ensemble-based classifiers. *Artificial Intelligence Review*, 33(1):1–39, Feb 2010.
- [83] CMS e-Lab. Energy, Mass and Momentum in High-Energy Physics. <https://www.i2u2.org/elab/cms/library/ref-mass-energy-momentum.jsp>.
- [84] Gregory Soyez. Pileup mitigation at the LHC: a theorist’s view. *Phys. Rept.*, 803:1–158, 2019.

- [85] N. Adam, J. Berryhill, V. Halyo, A. Hunt, K. Mishra. Generic Tag and Probe Tool for Measuring Efficiency at CMS with Early Data . http://cms.cern.ch/iCMS/jsp/openfile.jsp?tp=draft&files=AN2009_111_v1.pdf.
- [86]
- [87] J. Alwall, R. Frederix, S. Frixione, V. Hirschi, F. Maltoni, O. Mattelaer, H. S. Shao, T. Stelzer, P. Torrielli, and M. Zaro. The automated computation of tree-level and next-to-leading order differential cross sections, and their matching to parton shower simulations. *JHEP*, 07:079, 2014.
- [88] Thomas Junk. Confidence level computation for combining searches with small statistics. *Nucl.Instrum.Meth.*, A434:435, 1999.
- [89] Glen Cowan, Kyle Cranmer, Eilam Gross, and Ofer Vitells. Asymptotic formulae for likelihood-based tests of new physics. *Eur. Phys. J.*, C71:1554, 2011. [Erratum: *Eur. Phys. J.*C73,2501(2013)].
- [90] SM Higgs Combination. Technical Report CMS-PAS-HIG-11-011, CERN, Geneva, 2011.
- [91] S. Frixione, P. Nason, and C. Oleari. Matching nlo qcd computations with parton shower simulations: the powheg method. *JHEP*, 11:070, 2007.
- [92] S. Agostinelli et al. GEANT4—a simulation toolkit. *Nucl. Instrum. Meth. A*, 506:250, 2003.
- [93] Gionata Luisoni, Paolo Nason, Carlo Oleari, and Francesco Tramontano. $HW^\pm/HZ + 0$ and 1 jet at NLO with the POWHEG BOX interfaced to GoSam and their merging within MiNLO. *JHEP*, 10:083, 2013.

- [94] Comparison of nuisances for background only case, 350 GeV mass hypothesis.
http://rkamalie.web.cern.ch/rkamalie/feb12/Comparison_of_nuisances_expectedSignal0_350GeV.pdf
- [95] Comparison of nuisances for s+b case, 350 GeV mass hypothesis.
http://rkamalie.web.cern.ch/rkamalie/feb12/Comparison_of_nuisances_expectedSignal1_350GeV.pdf
- [96] k-factor for DY/Z. https://twiki.cern.ch/twiki/bin/viewauth/CMS/SummaryTable1G25ns#DY_Z
- [97] The LHC Higgs cross-section working group.
<https://twiki.cern.ch/twiki/bin/view/LHCPhysics/LHCHXSWG>.
- [98] Standard Model Cross Sections for CMS at 13 TeV.
<https://twiki.cern.ch/twiki/bin/viewauth/CMS/StandardModelCrossSectionsat13TeVInclusive>
- [99] SM Higgs production cross sections at $\sqrt{s} = 13$ TeV.
<https://twiki.cern.ch/twiki/bin/view/LHCPhysics/CERNYellowReportPageAt13TeV#ZHLLH>
- [100] NNLO+NNLL top-quark-pair cross sections.
https://twiki.cern.ch/twiki/bin/view/LHCPhysics/TtbarNNLO#Top_quark_pair_cross_sections
- [101] Single Top Cross sections. <https://twiki.cern.ch/twiki/bin/viewauth/CMS/SingleTopSigma>.
- [102] CMS GEN XSEC Task Force. <https://twiki.cern.ch/twiki/bin/viewauth/CMS/GenXsecTaskForce>
- [103] SM Higgs Branching Ratios and Total Decay Widths (update in CERN Report4 2016).
https://twiki.cern.ch/twiki/bin/view/LHCPhysics/CERNYellowReportPageBR#Higgs_2_gamma
- [104] Ryan Gavin, Ye Li, Frank Petriello, and Seth Quackenbush. W Physics at the LHC with FEWZ 2.1. *Comput. Phys. Commun.*, 184:208, 2013.

- [105] Stefano Frixione, Paolo Nason, and Giovanni Ridolfi. A Positive-weight next-to-leading-order Monte Carlo for heavy flavour hadroproduction. *JHEP*, 09:126, 2007.
- [106] J. Alwall, R. Frederix, S. Frixione, V. Hirschi, F. Maltoni, O. Mattelaer, H. S. Shao, T. Stelzer, P. Torrielli, and M. Zaro. The automated computation of tree-level and next-to-leading order differential cross sections, and their matching to parton shower simulations. *JHEP*, 07:079, 2014.
- [107] Gunter Zech. Upper Limits in Experiments with Background Or Measurement Errors. *Nucl. Instrum. Meth.*, A277:608, 1989.
- [108] A. L. Read. Presentation of search results: the CLs technique. *J. Phys. G: Nucl. Part. Phys.*, 28, 2002.
- [109] Rikkert Frederix, Emanuele Re, and Paolo Torrielli. Single-top t-channel hadroproduction in the four-flavour scheme with POWHEG and aMC@NLO. *JHEP*, 09:130, 2012.
- [110] Johan Alwall et al. Comparative study of various algorithms for the merging of parton showers and matrix elements in hadronic collisions. *Eur. Phys. J. C*, 53:473–500, 2008.
- [111] Serguei Chatrchyan et al. Determination of jet energy calibration and transverse momentum resolution in CMS. *JINST*, 6:P11002, 2011.
- [112] John M. Campbell and R. K. Ellis. MCFM for the Tevatron and the LHC. *Nucl. Phys. Proc. Suppl.*, 205-206:10, 2010.
- [113] Emanuele Re. Single-top Wt-channel production matched with parton showers using the POWHEG method. *Eur. Phys. J.*, C71:1547, 2011.

- [114] Gael L. Perrin, Pedro Fernandez Manteca. Muon Identification and Isolation Scale-Factors on 2016 Dataset. https://indico.cern.ch/event/611558/contributions/2465881/attachments/1407735/2151747/TnP_06_02_2017.pdf.
- [115] CMS Muon POG. Tracking SFs on the full 2016 data. https://twiki.cern.ch/twiki/bin/view/CMS/MuonWorkInProgressAndPagResults#Results_on_the_full_2016_data.
- [116] Gael L. Perrin. Double Muon trigger efficiency per-leg approach. https://indico.cern.ch/event/636555/contributions/2577291/attachments/1453162/2241537/TnP_DoubleMuSF_03_05_17.pdf.
- [117] Grace Dupuis. Collider Constraints and Prospects of a Scalar Singlet Extension to Higgs Portal Dark Matter. *JHEP*, 07:008, 2016.
- [118] Oleg Antipin, David Atwood, and Amarjit Soni. Search for RS gravitons via $W(L)W(L)$ decays. *Phys. Lett.*, B666:155–161, 2008.
- [119] A. Liam Fitzpatrick, Jared Kaplan, Lisa Randall, and Lian-Tao Wang. Searching for the Kaluza-Klein Graviton in Bulk RS Models. *JHEP*, 09:013, 2007.
- [120] Kaustubh Agashe, Hooman Davoudiasl, Gilad Perez, and Amarjit Soni. Warped Gravitons at the LHC and Beyond. *Phys. Rev.*, D76:036006, 2007.
- [121] CMS Higgs PAG. List of question for the preapproval checks. <https://twiki.cern.ch/twiki/bin/viewauth/CMS/HiggsWG/HiggsPAGPreapprovalChecks>.
- [122] CMS BTV POG. Supported Algorithms and Operating Points. https://twiki.cern.ch/twiki/bin/viewauth/CMS/BtagRecommendation80XReReco#Supported_Algorithms_and_Operati.

- [123] Albert M Sirunyan et al. Search for resonant and nonresonant Higgs boson pair production in the $b\bar{b}l\nu l\nu$ final state in proton-proton collisions at $\sqrt{s} = 13$ TeV. 2017.
- [124] Abdus Salam and John Clive Ward. On a gauge theory of elementary interactions. *Nuovo Cim.*, 19:165–170, 1961.
- [125] Steven Weinberg. A model of leptons. *Phys.Rev.Lett.*, 19:1264–1266, 1967.
- [126] Albert M Sirunyan et al. Evidence for the Higgs boson decay to a bottom quark-antiquark pair. 2017.
- [127] Aruna Kumar Nayak. Reconstruction of physics objects in the CMS detector. *PoS, CHARGED2012:010*, 2012.
- [128] Serguei Chatrchyan et al. Observation of a new boson at a mass of 125 GeV with the CMS experiment at the LHC. *Phys. Lett.*, B716:30–61, 2012.
- [129] Georges Aad et al. Observation of a new particle in the search for the Standard Model Higgs boson with the ATLAS detector at the LHC. *Phys. Lett.*, B716:1–29, 2012.
- [130] I. Belotelov, I. Golutvin, D. Bourilkov, A. Lanyov, E. Rogalev, M. Savina, and S. Shmatov. Search for ADD extra dimensional gravity in di-muon channel with the CMS detector. CMS Note 2006/076, 2006.
- [131] M. Aldaya, P. Arce, J. Caballero, B. de la Cruz, P. Garcia-Abia, J. M. Hernandez, M. I. Josa, and E. Ruiz. Discovery potential and search strategy for the standard model Higgs boson in the $H \rightarrow ZZ^* \rightarrow 4\mu$ decay channel using a mass-independent analysis. CMS Note 2006/106, 2006.

- [132] A. Brandt et al. Measurements of single diffraction at $\sqrt{s} = 630$ GeV: Evidence for a non-linear $\alpha(t)$ of the pomeron. *Nucl. Phys. B*, 514:3, 1998.
- [133] W. Buchmüller and D. Wyler. Constraints on SU(5)-type leptoquarks. *Phys. Lett. B*, 177:377, 1986.
- [134] CMS Collaboration. CMS technical design report, volume II: Physics performance. *J. Phys. G*, 34:995, 2007.
- [135] CMS Collaboration. Jet performance in pp collisions at $\sqrt{s}=7$ TeV. CMS Physics Analysis Summary CMS-PAS-JME-10-003, 2010.
- [136] S. Chatrchyan et al. The CMS experiment at the CERN LHC. *JINST*, 3:S08004, 2008.
- [137] Particle Data Group, J. Beringer, et al. Review of Particle Physics. *Phys. Rev. D*, 86:010001, 2012.
- [138] ALEPH, CDF, D0, DELPHI, L3, OPAL, SLD Collaborations, the LEP Electroweak Working Group, the Tevatron Electroweak Working Group, and the SLD Electroweak and Heavy Flavour Groups. Precision electroweak measurements and constraints on the Standard Model. 2010.
- [139] I. Bertram, G. Landsberg, J. Linnemann, R. Partridge, M. Paterno, and H. B. Prosper. A recipe for the construction of confidence limits. Technical Report TM-2104, Fermilab, 2000.
- [140] L. Moneta, K. Belasco, K. S. Cranmer, A. Lazzaro, D. Piparo, G. Schott, W. Verkerke, and M. Wolf. The RooStats Project. In *13th International Workshop on Advanced Computing and Analysis Techniques in Physics Research (ACAT2010)*. SISSA, 2010. PoS(ACAT2010)057.

- [141] Vardan Khachatryan et al. Search for the standard model Higgs boson produced through vector boson fusion and decaying to $b\bar{b}$. *Phys. Rev.*, D92(3):032008, 2015.
- [142] Performance of muon identification in pp collisions at $\sqrt{s} = 7$ TeV. Technical Report CMS-PAS-MUO-10-002, CERN, Geneva, 2010.
- [143] Serguei Chatrchyan et al. Performance of CMS muon reconstruction in pp collision events at $\sqrt{s} = 7$ TeV. *JINST*, 7:P10002, 2012.
- [144] CMS COLLABORATION. Particle-flow event reconstruction in CMS and performance for jets, taus, and E_T^{miss} . CMS Physics Analysis Summary CMS-PAS-PFT-09-001, CERN, 2009.
- [145] CMS COLLABORATION. Commissioning of the particle-flow event reconstruction with the first lhc collisions recorded in the cms detector. CMS Physics Analysis Summary CMS-PAS-PFT-10-001, CERN, 2010.
- [146] Vardan Khachatryan et al. Performance of Electron Reconstruction and Selection with the CMS Detector in Proton-Proton Collisions at $\sqrt{s} = 8$ TeV. *JINST*, 10(06):P06005, 2015.
- [147] CMS Collaboration. Search for pair production of first-generation scalar leptons in pp collisions at $\sqrt{s} = 7$ TeV. Submitted to *Phys. Rev. Lett.*, 2010.
- [148] CMS Collaboration. Performance of cms muon reconstruction in pp collision events at $\sqrt{s} = 7$ TeV. Submitted to *J. Inst.*, 2012.
- [149] ATLAS Collaboration. Search for the Higgs boson in the $H \rightarrow WW^{(*)} \rightarrow \ell^+ \nu \ell^- \bar{\nu}$ decay channel in pp collisions at $\sqrt{s} = 7$ TeV with the ATLAS detector. Submitted to *Phys. Rev. Lett.*, 2011.

- [150] Matteo Cacciari and Gavin P. Salam. Dispelling the N^3 myth for the k_t jet-finder. *Phys. Lett. B*, 641:57, 2006.
- [151] CMS Muon POG. Reference muon id, isolation and trigger efficiencies for Run-II. <https://twiki.cern.ch/twiki/bin/viewauth/CMS/MuonReferenceEffsRun2>.
- [152] John M. Campbell, R. Keith Ellis, Paolo Nason, and Emanuele Re. Top-pair production and decay at NLO matched with parton showers. *JHEP*, 04:114, 2015.
- [153] Ryan Gavin, Ye Li, Frank Petriello, and Seth Quackenbush. FEWZ 2.0: A code for hadronic Z production at next-to-next-to-leading order. *Comput. Phys. Commun.*, 182:2388, 2011.
- [154] Ye Li and Frank Petriello. Combining QCD and electroweak corrections to dilepton production in FEWZ. *Phys. Rev. D*, 86:094034, 2012.
- [155] Vardan Khachatryan et al. Event generator tunes obtained from underlying event and multiparton scattering measurements. *Eur. Phys. J. C*, 76(3):155, 2016.
- [156] Torbjorn Sjostrand, Stephen Mrenna, and Peter Z. Skands. A Brief Introduction to PYTHIA 8.1. *Comput. Phys. Commun.*, 178:852–867, 2008.
- [157] Rikkert Frederix and Stefano Frixione. Merging meets matching in MC@NLO. *JHEP*, 12:061, 2012.
- [158] Simone Alioli, Paolo Nason, Carlo Oleari, and Emanuele Re. NLO single-top production matched with shower in POWHEG: s- and t-channel contributions. *JHEP*, 09:111, 2009. [Erratum: JHEP02,011(2010)].

- [159] Michele de Gruttola, Rami Kamalieddin, Ilya Kravchenko, Lesya Shchutska. Search for resonant diHiggs production with $bbZZ$ decays with the $2b2l2\nu$ signature using 35.9/fb data of 2016 pp collisions at the LHC. http://cms.cern.ch/iCMS/jsp/openfile.jsp?tp=draft&files=AN2017_198_v17.pdf.
- [160] Chris Palmer. VHbb Electron Trigger and ID+ISO SFs for 2016 data. https://indico.cern.ch/event/604949/contributions/2543520/attachments/1439974/2216426/VHbb_TnP_SF_s_egamma_april.pdf#search=vhbb%20AND%20cerntaxonomy%3A%22Indico%2FExperiments%2FCMS%20meetings%2FPH%20%2D%20Physics%2FEgamma%22.
- [161] CMS JetMET group. Jet Energy Resolution. <https://twiki.cern.ch/twiki/bin/viewauth/CMS/JetResolution>.
- [162] CMS MET group. MET Corrections and Uncertainties for Run-II. <https://twiki.cern.ch/twiki/bin/viewauth/CMS/MissingETRun2Corrections>.
- [163] CMS MET group. MET Filter Recommendations for Run II. <https://twiki.cern.ch/twiki/bin/view/CMS/MissingETOptionalFiltersRun2>.
- [164] CMS EGM POG. Multivariate Electron Identification for Run2. <https://twiki.cern.ch/twiki/bin/viewauth/CMS/MultivariateElectronIdentificationRun2>.
- [165] Helge Voss, Andreas Höcker, Jörg Stelzer, and Frerik Tegenfeldt. TMVA, the toolkit for multivariate data analysis with ROOT. In *XIth International Workshop on Advanced Computing and Analysis Techniques in Physics Research (ACAT)*, page 40, 2007.

- [166] CMS Higgs WG. Documentation of the RooStats -based statistics tools for Higgs PAG. <https://twiki.cern.ch/twiki/bin/view/CMS/SWGuideHiggsAnalysisCombinedLimit>.
- [167] CMS Higgs WG. Binned shape analysis with the Higgs Combination Tool. https://twiki.cern.ch/twiki/bin/view/CMS/SWGuideHiggsAnalysisCombinedLimit#Binned_shape_analysis.
- [168] bbbb team. Search for resonant pair production of Higgs bosons decaying to bottom quark-antiquark pairs in proton-proton collisions at 13 TeV. <http://cms.cern.ch/iCMS/analysisadmin/get?analysis=HIG-17-009-pas-v5.pdf>.
- [169] Matteo Cacciari, Gavin P. Salam, and Gregory Soyez. The anti- k_t jet clustering algorithm. *JHEP*, 04:063, 2008.
- [170] Torbjörn Sjöstrand, Stephen Mrenna, and Peter Skands. PYTHIA 6.4 physics and manual. *JHEP*, 05:026, 2006.
- [171] C. Giunti and M. Laveder. Neutrino mixing. In F. Columbus and V. Krasnoholovets, editors, *Developments in Quantum Physics*. Nova Science Publishers, Inc., 2004.
- [172] Savas Dimopoulos, Stuart Raby, and Frank Wilczek. Proton decay in supersymmetric models. *Physics Letters B*, 112(2):133 – 136, 1982.
- [173] M. Della Negra, P. Jenni, and T. S. Virdee. Journey in the search for the higgs boson: The atlas and cms experiments at the large hadron collider. *Science*, 338(6114):1560–1568, 2012.

- [174] Lyndon R Evans and Philip Bryant. LHC Machine. *JINST*, 3:S08001. 164 p, 2008. This report is an abridged version of the LHC Design Report (CERN-2004-003).
- [175] Karsten Eggert, K Honkavaara, and Andreas Morsch. Luminosity considerations for the LHC. Technical Report CERN-AT-94-04-DI. CERN-LHC-Note-263. LHC-NOTE-263, CERN, Geneva, Feb 1994.
- [176] Oswald Gröbner. The LHC Vacuum System. (LHC-Project-Report-181. CERN-LHC-Project-Report-181):5 p, May 1998.
- [177] Thomas Lenzi. Development and Study of Different Muon Track Reconstruction Algorithms for the Level-1 Trigger for the CMS Muon Upgrade with GEM Detectors. Master’s thesis, U. Brussels (main), 2013.
- [178] Prospects for HH measurements at the HL-LHC. Technical Report CMS-PAS-FTR-18-019, CERN, Geneva, 2018.
- [179] Combination of searches for Higgs boson pair production in proton-proton collisions at $\sqrt{s} = 13$ TeV. Technical Report CMS-PAS-HIG-17-030, CERN, Geneva, 2018.
- [180] The CMS collaboration. Missing transverse energy performance of the cms detector. *Journal of Instrumentation*, 6(09):P09001, 2011.
- [181] Search for resonant double Higgs production with $bbZZ$ decays in the $b\bar{b}\ell\ell\nu\nu$ final state. Technical Report CMS-PAS-HIG-17-032, CERN, Geneva, 2018.
- [182] Werner Herr and B Muratori. Concept of luminosity. 2006.
- [183] Charles W. Misner, K. S. Thorne, and J. A. Wheeler. *Gravitation*. W. H. Freeman, San Francisco, 1973.

- [184] Serguei Chatrchyan et al. Description and performance of track and primary-vertex reconstruction with the CMS tracker. *JINST*, 9(10):P10009, 2014.